Real-Time Detection of Split Fronts Using Mesoscale Models and WSR-88D Radar Products

STEVEN E. KOCH

Department of Marine, Earth and Atmospheric Sciences, North Carolina State University, Raleigh, North Carolina

(Manuscript received 22 November 1999, in final form 27 June 2000)

ABSTRACT

A structured methodology for detecting the presence of split cold fronts in an operational forecast environment is developed and applied to a case in which a split front passed over a region of cold air damming in the southeastern United States. A real-time mesoscale model and various products from the WSR-88D—including the velocity–azimuth display wind profile (VWP) and hodograph products, plus a thermal advection retrieval scheme applied to the VWP data—are used to study this split front and an associated convective rainband that occurred on 19 December 1995.

Wet-bulb temperature and vertical motion forecasts at 700 hPa from the model revealed the arc-shaped split front 300–500 km ahead of the surface cold front. As this midtropospheric front passed across the surface warm front and entered the cold air damming region, model vertical cross-section analyses showed that it created a deep elevated layer of potential instability. Furthermore, an ageostrophic transverse circulation associated with the split front provided the lifting mechanism for releasing this instability as deep convection. Analysis of the absolute geostrophic momentum field provided greater understanding of the structure of the split front and a deep tropospheric frontal system to its west that connected with the surface cold front.

An ''S–inverted S'' pattern in the zero isodop on WSR-88D radial velocity displays indicative of wind backing above wind veering suggested the presence of the split front in the observations (as did the hodographs). Detection of the *passage* of the split front could be discerned from *temporal changes* in the vertical profile of the winds, namely by the appearance of midlevel backing of the winds in VWP time–height displays. Because of the subtlety of this backing and the need to be more quantitative, a temperature advection retrieval scheme using VWP data was developed. The complex evolving structure of the split front was revealed with this technique. Results from this retrieval method were judged to be meteorologically meaningful, to exhibit excellent time–space continuity, and to compare reasonably well with the frontal structures evident in the mesoscale model forecasts. The thermal advection scheme can easily be made to function in operations, as long as there is real-time access to level II radar data.

1. Introduction

Winter weather systems in the Carolinas, Virginia, and Georgia can be quite difficult to forecast owing to the extreme topographical variations that exert such a strong influence upon the weather in this region. Because the highest Appalachian Mountains exist nearby and the warm waters of the Gulf Stream are directly to the east, complex weather situations and a variety of winter precipitation types occur across the region (Keeter et al. 1995). A frequent cause of this complexity is cold air damming (CAD), wherein the Appalachians trap cold air along their eastern slopes (Richwein 1980; Forbes et al. 1987; Bell and Bosart 1988). The cold air dome is identifiable by a U-shaped pressure ridge in the sea level isobar pattern. A coastal front separating this cold, continental air from warmer maritime air is typically found along the eastern and southern boundaries of the damming region (e.g., Bosart et al. 1972; Riordan 1990). The coastal front is characterized by a strong mesoscale thermal gradient, an inverted trough in the sea level pressure field, and a pronounced cyclonic wind shift.

One of the primary processes for keeping the cold air in place is the southwestward acceleration of air associated with a force imbalance that results as cold air is retarded or blocked upon approaching the Appalachian Mountains from the east around the high pressure ridge (Forbes et al. 1987). Another process that maintains the damming is the adiabatic cooling of this stably stratified air as it is forced to ascend the mountain slopes. In some cases, diabatic cooling caused by evaporation of falling precipitation within the dry, cold air can enhance hydrostatic pressure rises (Fritsch et al.

Corresponding author address: Dr. Steven E. Koch, Department of Marine, Earth and Atmospheric Sciences, North Carolina State University, Campus Box 8208, Raleigh, NC 27695-8208.
E-mail: Steve_Koch@ncsu.edu

1992). Nonclassical (''in situ'') damming may also be initiated by *local* evaporational cooling processes and upslope-produced cloud cover. These processes create a mesoscale high pressure region within the cold pool. The enhanced northerly flow in the eastern and southern portions of this anticyclone increases low-level cold advection, resulting in further stabilization and greater damming.

Because of the extreme temperature contrast across the coastal front, the shallow nature of the cold dome, and the numerous mechanisms that affect CAD maintenance and erosion, one of the most difficult yet important forecast problems is the evolution and demise of the damming. Accurate forecasts of surface temperature, cloud cover, and precipitation type are highly dependent upon understanding and predicting these CAD mechanisms well. Operational numerical models tend to erode the cold dome prematurely (Keeter et al. 1995). Possible reasons that have been suggested for this continuing failure of the models include poor model initialization, insufficient vertical resolution, underrepresented terrain, and inadequate handling of cloud microphysics.

It is not the purpose of this paper to explore each of these many factors affecting the behavior of CAD events. Rather, we discuss a single *unexplored* mechanism that could either help to maintain or erode cold air damming, namely the passage of a cold frontal system aloft over a CAD region. If a significant rainband associated with the front aloft were to pass over the cold dome, several effects might ensue. If the air in the subcloud layer were quite dry, then as this precipitation fell through this layer, it should produce strong cooling, which could be an important factor in maintaining the damming event, at least locally. Alternatively, latent heat release within a highly convective rainband passing through a saturated atmosphere (in which evaporation is insignificant) might cause hydrostatic pressure falls at the surface in the cold air and along the coastal front. This could possibly result in the formation of a spurious mesoscale cyclone there. The isallobaric fall center would occur just ahead of the mesocyclone along the coastal front. Since isallobaric flow is by nature convergent, then this implies that frontogenesis would be enhanced along this front downstream (to the northeast) of the cyclone. The culmination of this hypothetical process would then be that the coastal front reforms inland over the Carolina Piedmont, leading to the sudden erosion of the cold air. On the other hand, these processes may largely offset one another, leading to little or no noticeable effect on the cold dome structure.

Before we can begin to address these questions, operationally useful techniques must first be developed for detecting and diagnosing cold fronts in the midtroposphere. A shallow cold dome should prevent the downward penetration of the cold front aloft to the surface, resulting in few clues to its presence other than perhaps a weak pressure trough and associated wind shift (Neiman et al. 1998). Therefore, methods that do not rely upon surface data for detecting these fronts must be utilized.

The current study will show that two essential tools allowing this to be achieved are the Weather Surveillance Radar-1988 Doppler (WSR-88D) and mesoscale models. First, the WSR-88D network enables meteorologists to determine whether organized mesoscale bands may be the dominant producer of significant precipitation in CAD events. This suggestion contrasts with earlier (pre-WSR-88D) studies suggesting that general overrunning (isentropic lift) is dominant (Gurka et al. 1995). Second, we seek to determine whether the velocity–azimuth display (VAD) wind profile (VWP) product (Klazura and Imy 1993) may be useful for helping forecasters to visualize the presence of cold fronts aloft. The basis for this suggestion is that frontal systems are coupled to jets through the thermal wind relationship.

Another powerful tool in the arsenal of today's weather forecaster is the mesoscale model. Constantly increasing advances in computing power have made running large domain mesoscale models in real time a reality. Even though many National Weather Service offices do not yet have access to the full 32-km-resolution Eta Model, many are benefiting from collocated or nearby universities that are running real-time mesoscale models with sophisticated physics at high resolution on workstations (Cotton et al. 1994; Mass and Kuo 1998).

The current study uses conventional data, regional radar mosaics, a real-time mesoscale model run at North Carolina State University, and various products from the WSR-88D radar, including a new thermal advection retrieval product, to investigate a split front that passed over a CAD region. This case is examined in section 3, following some background material on split fronts and cold fronts aloft in section 2. Interactions between the split front and cold air damming are discussed in section 4.

2. Background

A fundamental property of fronts in the atmosphere is that they display locally large horizontal temperature gradients, static stability, absolute vorticity, and vertical wind shear. Upper-level and surface frontal zones may be distinguished by the differing processes that generate them. Irrespective of whether geostrophic deformation or tilting processes are the cause, upper-level and surface frontal zones both exhibit vertical circulations arising as the consequence of the resultant frontogenesis (Shapiro 1981). Upper-level fronts result from a process known as tropopause folding, which is best revealed by the downward extrusion of stratospheric levels of potential vorticity deep into the troposphere, though usually not to the lower troposphere (Reed 1955; Reed and Danielsen 1959).

Imperfect numerical models and satellite or radar im-

agery must be interpreted in terms of conceptual models to be used effectively in issuing a weather forecast. Neither the upper-level front model nor the Norwegian frontal model can fully explain all observations of actual frontal systems in midlatitudes. In particular, an explanation is needed for the occurrence of squall lines and other mesoconvective systems that form at least 200 km ahead of surface cold fronts and pass through cold air damming regions with little loss in vigor. Crawford (1950) established nearly 50 years ago that early spring squall lines ''of any importance'' in the southeastern United States form *without exception* when strong cold advection at 700 mb advances over the axis of a warm tongue at 850 mb and well ahead of surface cold fronts. This observation suggests that cold fronts above the surface may be the responsible agent in most such instances.

Browning (1985) employed the conveyor belt paradigm[1] to attribute prefrontal squall lines in the United States to split cold fronts (Browning and Monk 1982), so-named because of the separate existence of the upper cold front ahead of the surface cold front. Split cold fronts are essentially katafronts, since air within the warm conveyor belt ascends in a forward sloping fashion ahead of the surface cold front (Fig. 1a). Low wet-bulb potential temperature (θ_w) air within the dry conveyor belt overruns the warm conveyor belt, creating potential instability that is realized as a convective rainband well ahead of the surface cold front. Little or no precipitation occurs in the shallow warm air immediately ahead of the surface cold front because the deep layer of dry air created by the passage of the split front limits the depth of the moist layer (Fig. 1b).

Hobbs et al. (1990) have proposed that the cold front aloft model (CFA) can explain prefrontal squall lines east of the Rocky Mountains and, in some cases, even to the East Coast. The primary distinction between a CFA and a split front is that a split front is a forward-sloping upper cold front present over the warm sector ahead of a surface cold front, whereas the CFA is present ahead of a lee trough or dryline. Thus, ''in these systems the region analogous to the classic warm sector of a warm occlusion is located west of the surface position of the lee trough, not east of it as required by the split-front model'' (Locatelli et al. 1995, p. 2659). According to Browning and Roberts (1996), split cold fronts resemble warm occlusions, in that relatively low-θ_w air overruns the surface cold front. However, in an idealized occlusion, high-θ_w air does not exist in the layer close to the ground, whereas in a split cold front, a shallow layer of relatively high-θ_w air remains at low levels between the surface warm and cold fronts. This is what is depicted in the conceptual cross section in Fig. 1b.

Split fronts and cold fronts aloft are both best seen in vertical cross sections of either wet-bulb potential temperature or equivalent potential temperature, and in fact, the change in humidity apparently is the strongest indicator of their presence. Nevertheless, it would be inappropriate to define any feature as a front solely on this basis; thus, a significant horizontal temperature gradient must also exist. The CFA is thought to form as the consequence of the combined effect of the blocking by the Rocky Mountains of the lower-tropospheric part of a Pacific cold front and adiabatic warming by strong descent over the lee slopes. Thus, the idea is that the surface cold front is eroded while the midlevel cold advection continues to progress eastward unimpeded over the plains states. This orographic forcing is not a requisite feature in the split-front model, which was originally developed in the United Kingdom.

Signatures useful for detecting a CFA in satellite, model, and conventional data were developed by Hobbs et al. (1990). They are summarized here with some modification in order that they can be generalized to the split front, which is the topic of the current paper:

- the main precipitation band or cloud band is ~200–300 km ahead of the surface cold front, with a rapid decrease in cloud top heights behind the split front (caused by the dry conveyor belt),
- the leading edge of cold advection at 700 hPa is aligned with the cloud band,
- cross sections normal to the front show a strong horizontal gradient of θ_w and a pattern of backing winds above veering winds in the midtroposphere ahead of the cold front at the surface,
- there is a concentrated region of strong absolute momentum gradients along the midtropospheric cold front corresponding to the strong vertical and lateral shears (this is discussed in detail immediately below),
- numerical models indicate a band of strong upward motion well ahead of the surface trough or cold front and parallel with the midtropospheric cold front, and
- radial velocity fields from WSR-88D plan-position indicator (PPI) displays show a signature indicative of geostrophic cold advection overlying warm advection (this is discussed later).

Absolute geostrophic momentum appears on the list of Hobbs et al. (1990) for the following reason. If we define the positive y axis to point in the direction of the cold air, denote the alongfront component of the geostrophic wind by U_g, and the Coriolis parameter by f, then the absolute geostrophic momentum

$$M_g = U_g - fy \tag{1}$$

can be used to define frontal zones (Eliassen 1962). Provided that the alongfront component of the wind is approximately geostrophic, M_g can singly describe two-dimensional frontal zones in terms of their absolute geo-

[1] The conveyor belt paradigm is based on the notion that the main airflow in a midlatitude cyclone can be described in terms of system-relative flow on isentropic surfaces under the assumption that the cyclone does not evolve rapidly [the ''frozen wave assumption'' as defined by Carlson (1980)].

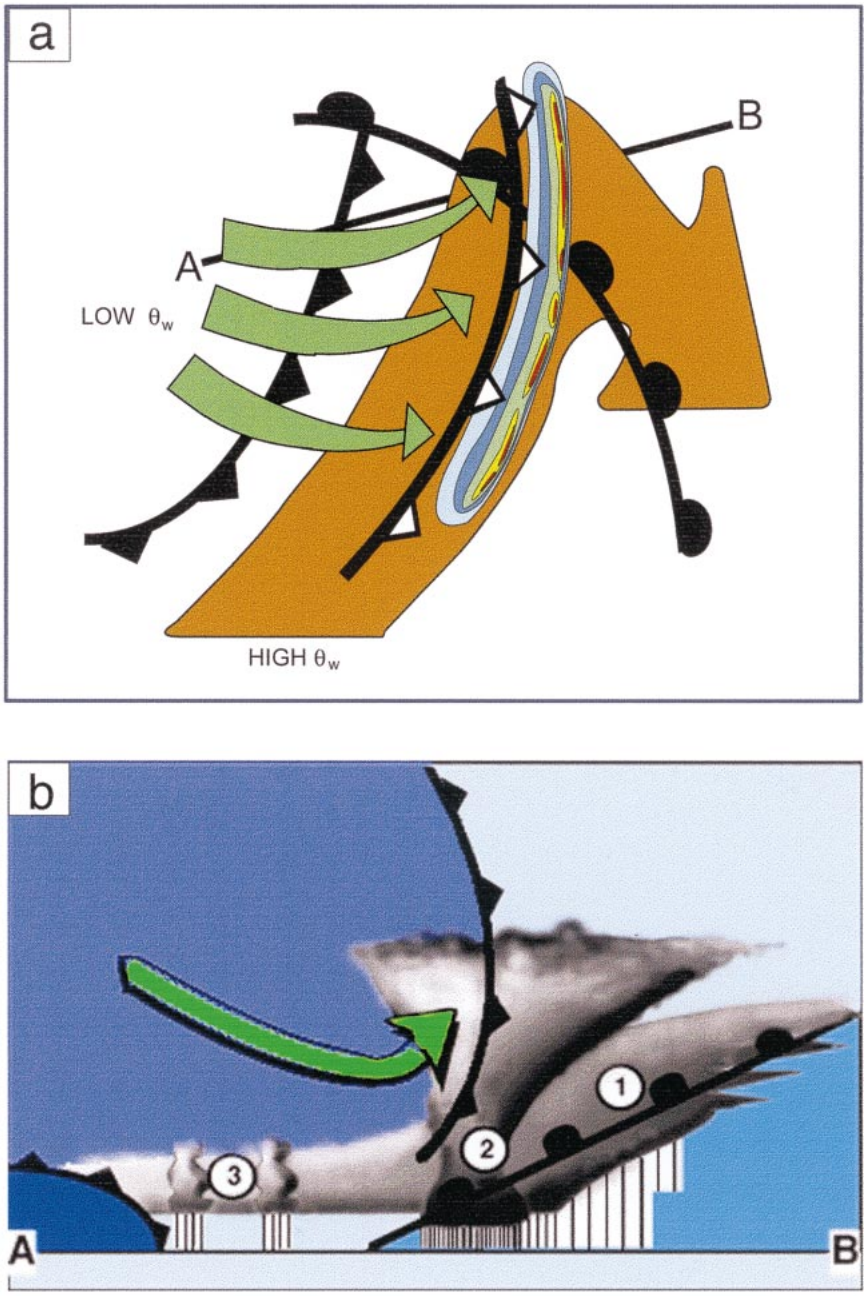

FIG. 1. (a) Schematic plan view of a split front (after Browning and Monk 1982). The broad brown arrow depicts the warm conveyor belt (high-θ_w air), which gently rises in an isentropic coordinate system relative to the moving cyclone. The green arrows represent the flow of low-θ_w air within the dry conveyor belt, which descends while overrunning the warm conveyor belt. The leading edge of the low-θ_w air marks the position of the split cold front (open pips), just ahead of which appears a rainband. Surface fronts are shown by standard symbols. (b) Vertical cross section along A–B showing 1) region of light precipitation along warm front, 2) intense precipitation produced by split-front rainband, and 3) shallow, light precipitation occurring in the warm sector ahead of the surface cold front. The dry conveyor belt is depicted by the broad green arrow behind the split front.

strophic vorticity ($-\partial M_g/\partial y = f - \partial U_g/\partial y = \eta_g$) and horizontal temperature gradient, which is related to the vertical shear through the thermal wind relationship ($\partial M_g/\partial p = \partial U_g/\partial p \propto \partial\theta/\partial y$). Thus, the product of these two quantities, an ad hoc parameter that is here defined as the momentum gradient product,

$$\left|\frac{\partial M_g}{\partial p}\frac{\partial M_g}{\partial y}\right|, \tag{2}$$

is a powerful parameter for highlighting the existence of frontal zones in cross sections.

The passage of a CFA or split front creates not only potential instability, but also the mechanism by which this instability may be released. Semigeostrophic theory predicts that a thermally direct circulation should occur if active frontogenesis is present within the frontal zone (Keyser and Shapiro 1986). Such vertical motion might be capable of lifting the warm air ahead of the front to saturation and, thus, trigger the formation of a band of elevated convection not just ahead of the surface front or drytrough, but also above a region of shallow cool air (such as cold air damming). Thus, the CFA or split-front conceptual model addresses a difficult forecasting dilemma. Locatelli et al. (1995) and Neiman et al. (1998) discuss a case that occurred over Oklahoma, in which a line of severe thunderstorms developed as a CFA within the ''dry slot'' of a cyclone passed over cool air at the surface. The low-level cool air was uncoupled from the cold front aloft. Rainbands at the leading edge of a split front or CFA have been noted in other cases in the mid-Atlantic region (Locatelli et al. 1989; Martin et al. 1990, 1992). Businger et al. (1991) studied an eroding cold air damming situation in which severe weather developed as a CFA overtook a Piedmont front in the Carolinas.

All of the above cases benefited from special surface and upper-air observations taken during mesoscale field experiments. The case presented below uses only operationally available data. In so doing, this study serves to illustrate the tremendous advantage gained by forecasters and researchers alike by having the full Next Generation radar network in place and access to a real-time mesoscale model. The kinds of frontal systems that are demonstrated by this case study on the East Coast may in some cases have had their origins in a CFA structure when they were over the plains states [as in the case presented by Locatelli et al. (1989)]. Yet, by the time the upper cold front has advanced to the East Coast, invariably the drytrough has been overtaken by an arctic or Canadian cold front that has swept southward over the plains and then eastward. The result is a structure that looks more like the split-front model. For these reasons, the split front terminology is used hereafter in this paper.

3. Case study

The case presented here, which occurred on 18–19 December 1995 in the southeastern United States, involved the passage of a split front over a region of cold air damming and the production of a band of strong thunderstorms ahead of this front. Regional radar mosaics, operationally available and nonconventional products from the WSR-88D, a real-time mesoscale model, and conventional data are used in this study. Surface data were objectively analyzed using the GEMPAK Barnes scheme with a numerical convergence factor $\gamma = 0.3$ for the second pass (Koch et al. 1983). The radar mosaics were constructed from individual WSR-88D composite reflectivity displays from radar sites at Birmingham, Alabama (KBMX); Atlanta, Georgia (KFFC); Greenville–Spartanburg, South Carolina (KGSP); Raleigh, North Carolina (KRAX); and Morehead City, North Carolina (KMHX). Although the reflectivity mosaics identified the split-front rainband, the VAD from the WSR-88D (Klazura and Imy 1993) was the primary observing tool for detecting the presence of the split front itself. VAD was used both in the form of the VWP and wind hodograph products. In addition, geostrophic thermal advection fields were obtained from the VWP (explained below) to aid in the identification of the structure of the split front.

The model used in this study is the hydrostatic Mesoscale Atmospheric Simulation System (MASS) run in real time at North Carolina State University. MASS was initialized at 0000 UTC 19 December 1995 from the concurrent 80-km resolution Eta Model simulation. By using the initial state of the Eta Model (Rogers et al. 1995), rather than a prior forecast from MASS or Eta, MASS benefited from the sophisticated Eta Data Assimilation System (Rogers et al. 1996) while not suffering from prior model forecast errors. Static initialization was performed on the coarse MASS grid (45-km resolution), and a 36-h forecast was made. The coarse grid was used in the present study; although a nested fine mesh (15 km) grid is also available from the real-time MASS system, it encompasses too small of an area for this study. Terrain data were derived from the U.S. Central Intelligence Agency 5-min (~9 km) global dataset. Sea surface temperatures were taken from a 20-km resolution global climatological dataset that is updated biweekly. Model physics included the Blackadar boundary layer scheme, a Kuo–Anthes cumulus parameterization scheme modified to include moist convective-scale downdrafts, and a prognostic microphysical parameterization for cloud water, cloud ice, rainwater, and snow. Additional details about MASS are given in Kaplan et al. (1982). Koch et al. (1985) performed an evaluation of an early version of this model. More recent changes to MASS are described by Manobianco et al. (1994, 1996).

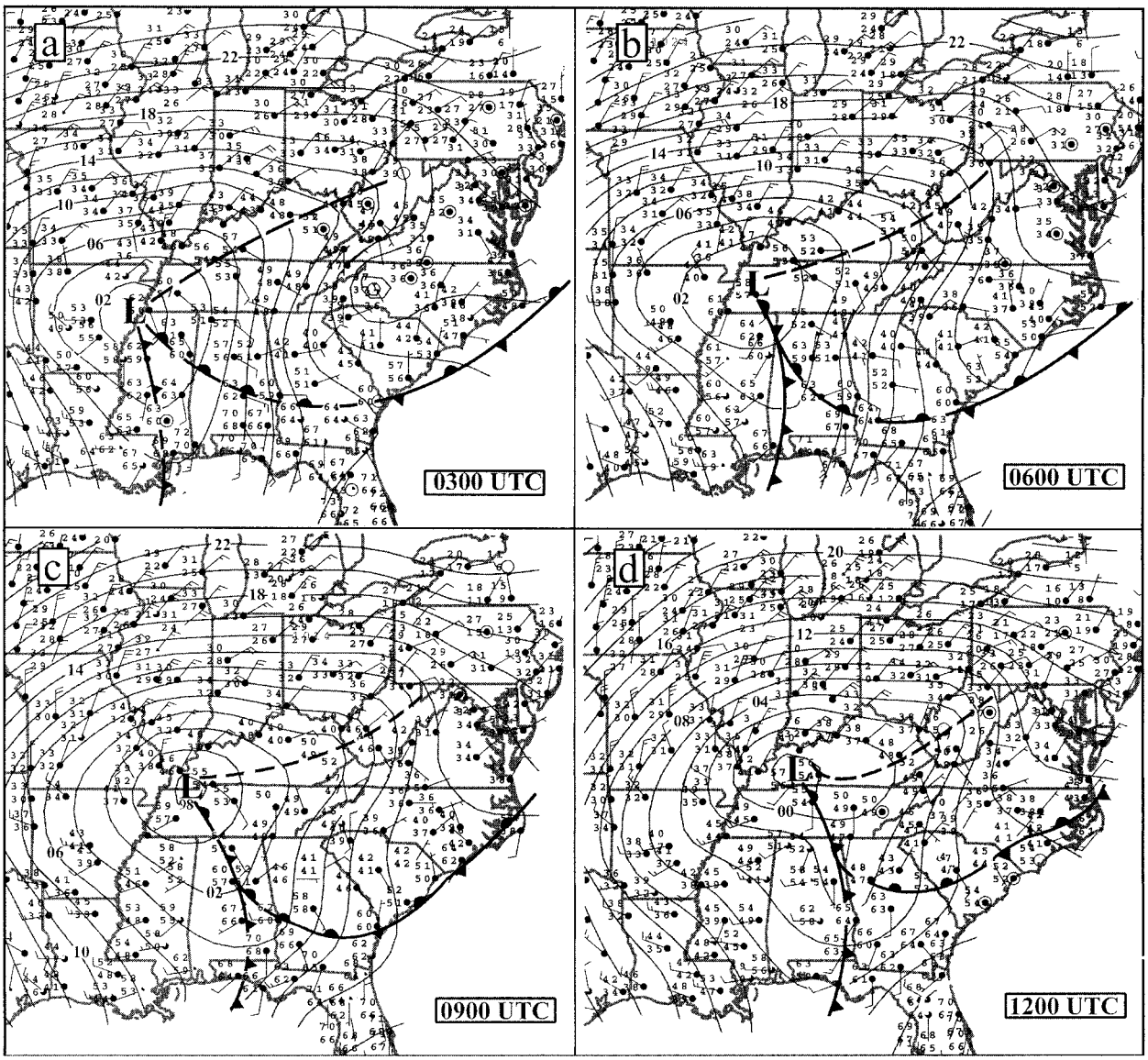

FIG. 2. Surface analyses at (a) 0300, (b) 0600, (c) 0900, and (d) 1200 UTC 19 Dec 1995. Objectively analyzed isobars (solid lines) are shown at 2-hPa intervals. Temperature and dewpoint (°F) are plotted at the stations.

a. Observational analysis

A strong high pressure system over the Great Lakes provided cold northeasterly flow throughout this CAD event. The primary surface cyclone traveled slowly from Memphis at 0300 UTC to southwestern Kentucky by 1200 UTC (Fig. 2). Note the U-shaped pressure ridge from Maryland southward into the Carolinas, which reveals the presence of cold air damming. Surface temperatures in North Carolina remained virtually constant over this 9-h period as clouds and precipitation blanketed the region. Precipitation over the southeastern United States was in the liquid form and was generally light, with the important exception being when a convective rainband associated with the split front (discussed below) passed over the region. The Carolina coastal front made very little progress inland until 1200 UTC; thereafter, it advanced no farther, most likely because diabatic cooling helped to reinforce the cold air.

A similar time sequence of the enhanced infrared satellite imagery (Fig. 3) reveals a large-scale comma cloud typically associated with midlatitude cyclones, with the head of the comma over Missouri and the tail having a rather convective appearance over Alabama, western Georgia, and the Florida panhandle. Judging on this basis alone, one would be hard-pressed to identify a rainband significantly in advance of the surface front. In fact, there is no evidence in either this window channel imagery or the water vapor channel (not shown) of

a dry intrusion sweeping well ahead of the occluded front that is characteristic of cold fronts aloft and split fronts. However, rearward advection of cirrostratus cloud material from cumulonimbus clouds within the convective band would disguise the presence of a dry conveyor belt in the midtroposphere.

Closer inspection of the infrared imagery suggests the likely presence of deep convection north of the warm front in Georgia and well ahead of the surface cold front at 0300 and 0600 UTC. In fact, the radar mosaics (Fig. 4) reveal that an organized mesoconvective system progressed from central Georgia at 0300 UTC, to western South Carolina at 0600 UTC, though it became less organized as it weakened in its further progression across the Carolinas. The cold cloud tops in the infrared imagery do not correspond very well to the presence of strong convection at all times, such as in eastern Alabama at 0600 UTC. For this reason, greater reliance should be placed on the radar than the satellite imagery in this situation where deep clouds are present across a large portion of the southeastern United States and mask the presence of the strongest embedded convection. The separation of this prefrontal band of organized convection from the surface cold front increases from 400 km at 0300 UTC to 580 km by 1200 UTC, at which time its remnants are located in southeastern North Carolina. Given that an organized mesoconvective system has been identified well ahead of the surface front, we proceed next to examine whether a mesoscale forcing mechanism for this rainband can be identified in numerical model forecast fields.

b. Mesoscale model analyses

MASS model forecast fields of mean sea level pressure and 10-m winds (Fig. 5) show an evolving situation similar to that observed (Fig. 2). The characteristic CAD pressure wedge and coastal front are visible in the isobars and wind field at 0300 UTC. However, the shape of the isobars suggests that the forecast CAD is not as strong as that observed. Comparison of the observed and forecast fields 9 h later (1200 UTC) indicates that the model prematurely eroded the CAD (as is typical of most models), particularly across North Carolina. Of greater importance for the current study is that the surface cold front in the Gulf states and attendant primary cyclone were predicted quite well (though slightly too slow). Thus, the MASS model produced a reasonable forecast of the surface situation, with the exception of premature erosion of some of the CAD region.

The cause for this premature CAD erosion is made clear upon closer inspection. MASS incorrectly simulated a weak mesoscale cyclone to develop along the warm front and then propagate from northeastern Georgia at 0900 UTC to central North Carolina at 1200 UTC. Synoptic-scale cyclogenesis often marks the dissipating phase of cold air damming (Bell and Bosart 1988), but a mesoscale frontal wave is a different phenomenon. As discussed earlier, since the isallobaric fall center occurs just ahead of the mesocyclone along the warm front, frontogenesis was enhanced to the northeast of the cyclone along this front, resulting in the sudden reformation of the coastal front over the Piedmont region and the dislodgment of the cold air. There is no evidence for a wave cyclone and associated retreat of the cold air in the surface observations. However, careful inspection of the surface winds suggests the presence of a weak cyclonic circulation in northwestern South Carolina at 0900 UTC (Fig. 2c). By 1500 UTC, secondary cyclogenesis had begun along the North Carolina coastal front. This cyclone rapidly strengthened to a ''bomb'' status in the subsequent 24 h in association with increased cyclonic vorticity advection over the damming region. Large amounts of snow were dumped across the Northeast by this ensuing storm.

Dry- and wet-bulb temperatures, winds, and vertical motions predicted by the MASS model at 700 hPa are shown in Fig. 6 at the same four times displayed in the previous figures. A well-defined frontal system is revealed in the wet-bulb temperature fields and, to a lesser degree, in the dry-bulb temperature forecasts, with an attendant arc-shaped band of strong upward motions along most of its extent. This feature is 300–500 km ahead of the forecast surface cold front and displays a character highly suggestive of a split front. The associated arc-shaped band of upward motion shares strong similarity in appearance and location to the swirling comma cloud field about the cyclone seen in the infrared satellite imagery (Fig. 3).

The split front cuts nearly perpendicular to the warm front in northern Georgia at 0600 UTC (Fig. 6c) and in the Carolinas at the later times, and also crosses the warm front in the Ohio River Valley. Notice that the weak surface cyclone predicted by the model appears precisely at the location where the split front crosses the southernmost warm front. The dynamical explanation for this feature begins with the observation that a 55–65-kt mesoscale jet at 700 hPa was consistently found at this intersection. Coexistence of this wind maximum with the enhanced horizontal temperature gradient at the leading edge of the split front is consistent with the thermal wind relation.[2] A local maximum of cyclonic vorticity advection associated with the mesoscale jet contributes to both the strong rising motion near the point of intersection of the split front with the surface warm front, and to the surface pressure falls responsible for the appearance of the weak frontal cyclone.

Many cross-sectional analyses were constructed perpendicular to the split front and the associated rainband to understand their interrelationships. The cross sections shown here are taken from Little Rock, Arkansas (LZK),

[2] The strong temperature gradient present farther to the west in Mississippi during the early part of the forecast period also is associated with a jet and is discussed later.

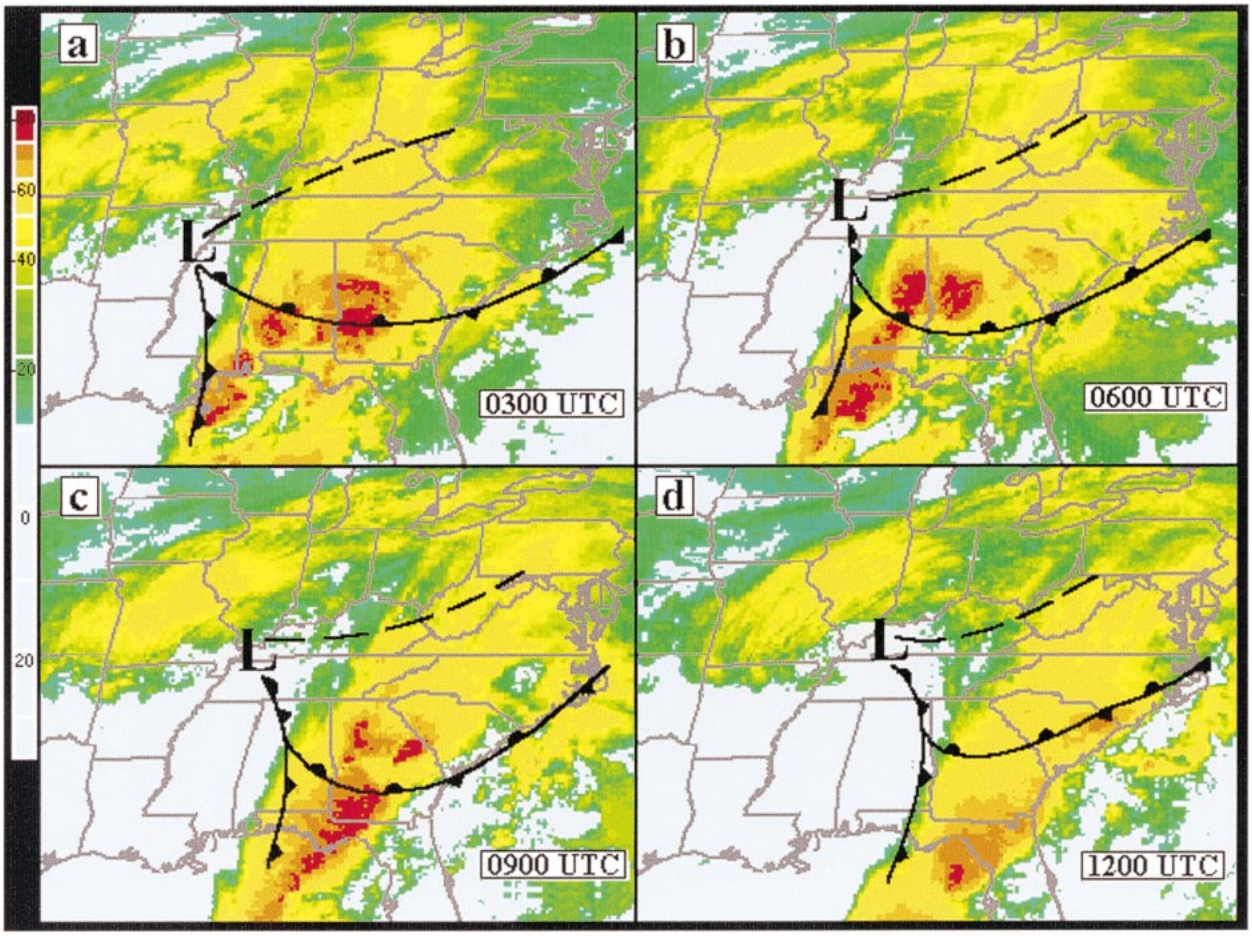

FIG. 3. Color-enhanced infrared Geostationary Operational Environmental Satellite imagery and surface analyses at the same four times as in Fig. 2. Color bar denotes blackbody temperature (°C).

to Elizabeth City, North Carolina (ECG). These cross sections were chosen because they passed through the strongest vertical motion along the split front, the CAD region, and also near to the radar sites available for this study (section 3d).

The isentropic cross section (Fig. 7) shows two frontal systems. First, a deep tropospheric front makes its appearance in the plane of this cross section by 0600 UTC. The center of this dome of cold air is evident by 1200 UTC, ~200 km east of LZK. Cold advection (shaded) behind this frontal system exhibits maxima above 600 hPa and below 700 hPa, with the lower one being associated with the surface cold front. The second frontal system—the split front—displays a mesoscale dipole of cold and warm advection in the midtroposphere that travels eastward at a steady speed of 20 m s^{-1} (72 km h^{-1}). This dipole is evident at various levels at the individual forecast times, but it is always present somewhere in the 400–700-hPa layer. The split front is analyzed at the point where the isentropes in this layer begin to slant upward in an essentially continuous fashion toward the west (the left). By contrast, a gravity wave would display isentropes that undulate up- and downward. It is this nature to the isentropes, as well as the strong horizontal temperature gradient, and the associated mesoscale jet at 700 hPa, which lead to the conclusion that a cold front was present. Admittedly, the temperature contrast was weaker than the gradients in wet-bulb temperature (Fig. 6), but this is characteristic of split fronts, as discussed by Browning and Roberts (1996).

Although the ''ballooning'' in the isentropes in the 550–350-hPa layer at 0600 UTC implies that latent heating was released along this front, this convection vanishes within the next 3–4 h. Neither does the structure in the isentropes suggest convection was present at 0300 UTC. Thus, we find no cause to suggest that convection alone produced this feature.

The split front is even more apparent in the cross sections of equivalent potential temperature θ_e (Fig. 8). Two regions of strong horizontal gradient in θ_e are evident: one associated with the split front and the other with the deep tropospheric frontal system. However, the influence of these frontal systems on the stability of the

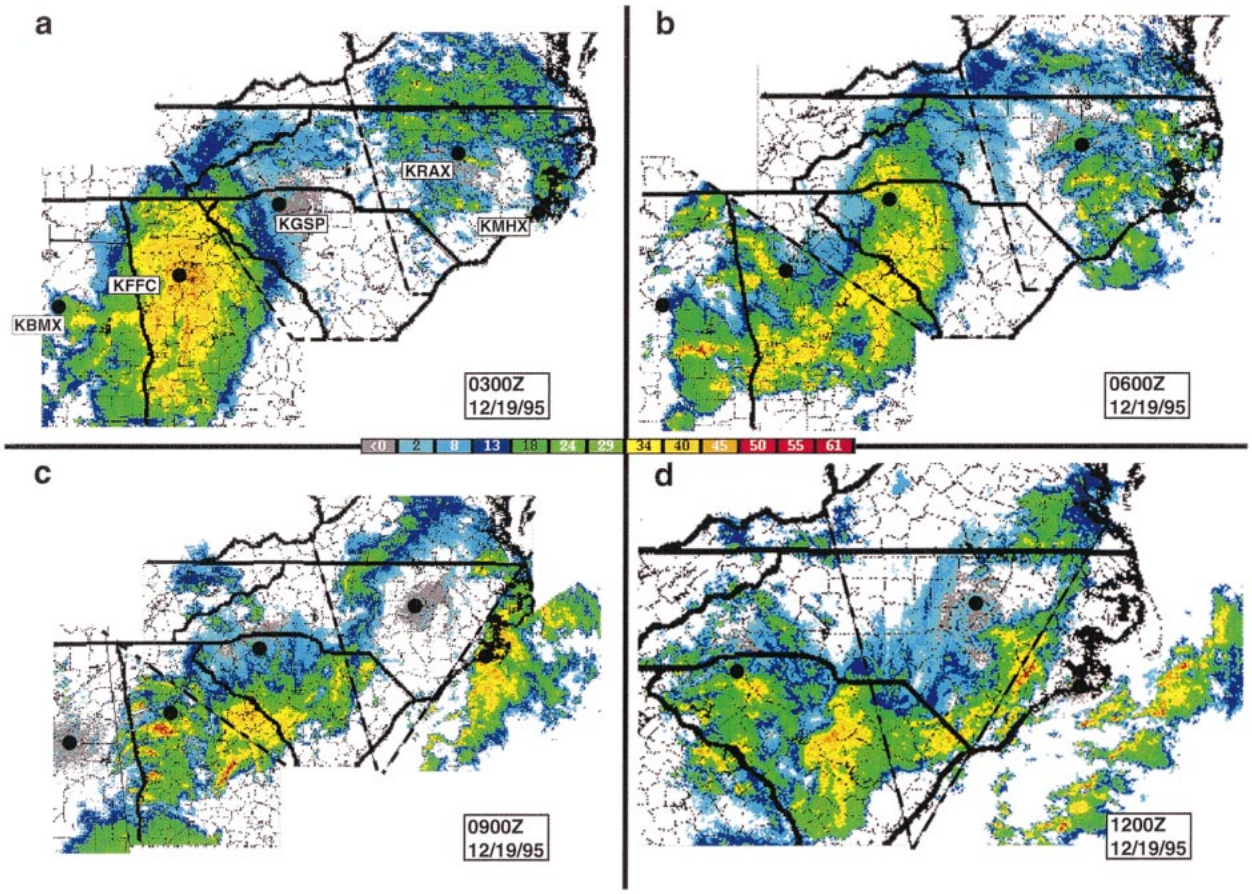

FIG. 4. Mosaics of radar composite reflectivity at the same times as in Fig. 2. Radar reflectivity values (dBZ) are given in the color bar. Dotted black lines are counties. Dashed lines depict borders between the individual radar ''panels'' composing the mosaic (radar sites used in this analysis are shown by their station IDs). Note difference in scale in (d).

atmosphere is drastically different. As the dry, cool air behind the split front advances over warm, moist air, an elevated region of potential instability ($\partial\theta_w/\partial z < 0$) is created that spans a large volume of the troposphere; by contrast, only a shallow layer of potential instability near the surface is created by the deeper front. It is important to observe that the destabilization created by the passage of the split front is strongest at 0600 UTC (over northern Georgia), which is when the implied convection in Fig. 7 was most apparent, and becomes nearly imperceptible by 1200 UTC (over North Carolina). This model behavior is generally consistent with the observed morphology of the precipitation patterns seen in the radar mosaics (Fig. 4), and is shown below to also be consistent with interpretations of the radar VAD analyses.

It was mentioned earlier that the momentum gradient product (2) is a very useful parameter for helping to identify the existence of frontal systems, provided that they are in thermal wind balance. This field does indeed do an excellent job in highlighting the existence and structure of the deep tropospheric front and its connection with the surface cold front (Fig. 9). The momentum gradient product also is helpful in isolating the simulated split front, its depth, the fact that it is generally strongest in the 600–700-hPa layer, and that it maintains coherence throughout the 9-h period.

Strong upward motion occurs along the leading edge of the forecast split front from 0300 to 1200 UTC (Fig. 10). This thermally direct frontal circulation is associated with active frontogenesis,[3] with the rising branch of the circulation acting upon saturated air (shaded), much of which is also potentially unstable (Fig. 8). Thus, the split front not only creates the potential instability, but also provides the forcing mechanism for releasing this instability in the form of a band of elevated convection. An impressive horizontal gradient of relative humidity is present just behind the split front, which is the reason why the θ_e and wet-bulb temperature fields

[3] This transverse circulation is composed of the horizontal wind component in the cross-front plane relative to the motion of the front and the total vertical motion.

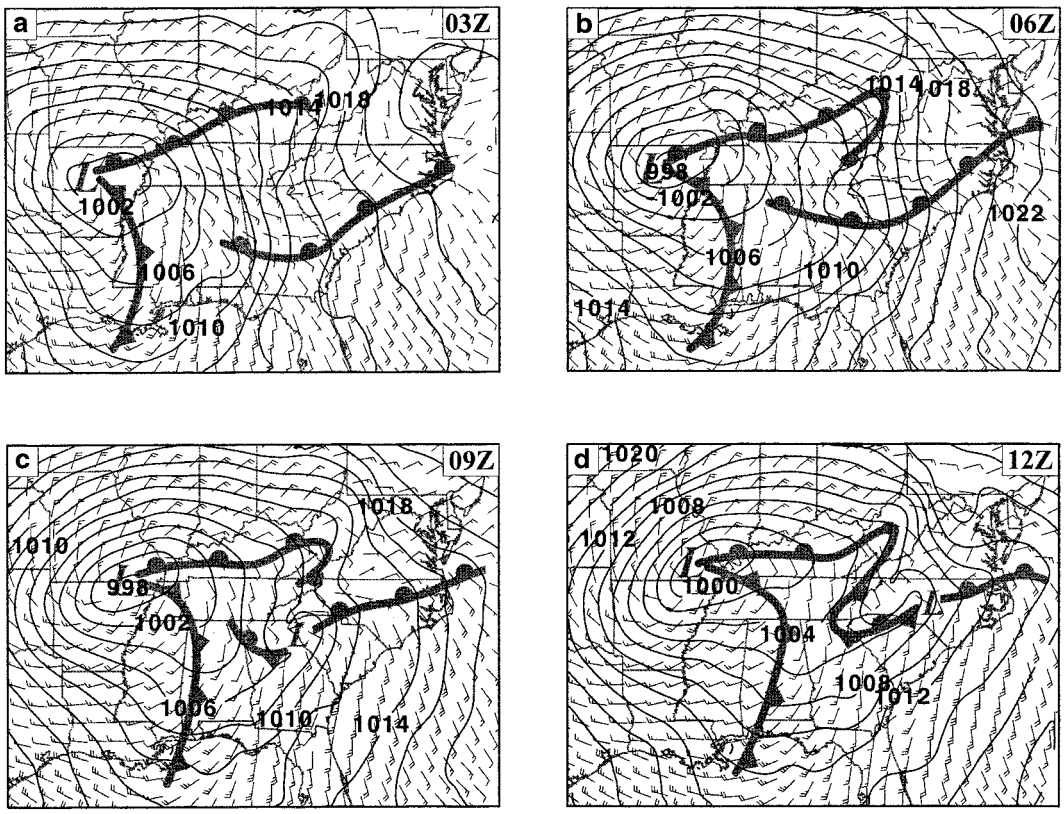

FIG. 5. MASS model forecasts of ''surface'' fields [2-hPa isobars of mean sea level pressure (solid lines) and l0-m winds] at the same times as in Fig. 2. Surface fronts are shown by standard symbols. Wind barb nomenclature is conventional (full barb = 5 m s^{-1}, half barb = 2.5 m s^{-1}, flag = 25 m s^{-1}).

did a better job at defining the presence of the split front than did the temperature field. Note also the presence of a secondary region of moisture just ahead of and above the surface cold front. However, because this feature occurs above a much shallower region of potential instability, it is much more difficult for deep convection to develop here compared to ahead of the split front, just as in the conceptual model (Fig. 1b).

c. Radar detection of the split front

Frontal systems are coupled to jet streaks in the atmosphere, provided that they are in thermal wind balance, which is equivalent to assuming geostrophic and hydrostatic equilibrium. Geostrophic cold and warm advection can be easily inferred from backing and veering of the winds with height, respectively. The WSR-88D provides several real-time tools of use to the forecaster who desires to know of such thermal advection patterns. First, radial velocity displays at various elevation angles can be inspected for the existence of an ''S–inverted S'' pattern in the zero isodop (where an isodop is a line of equal radial velocity on the radar display). The wind direction is given by a line drawn perpendicular to a radial at the point where that radial intersects the zero isodop. Thus, an S-shaped isodop pattern at constant elevation angle indicates veering winds with height (or radar range) for a horizontally homogeneous atmosphere (Brown and Wood 1983). Similarly, backing winds are indicated by the appearance of an inverted-S zero isodop. An idealized radial velocity display for this situation (Fig. 11a) indicates veering of winds from a southerly to a westerly direction with height (the inner portion of the zero isodop), overlain by backing of winds from westerly to southerly. Accordingly, geostrophic warm advection at low levels and cold advection aloft may be implied from an S–inverted S pattern. This technique was first employed for the detection of cold fronts aloft by Hobbs et al. (1990).

As the split front rainband passed through west-central South Carolina, the KGSP radar displayed an S–inverted S pattern (Fig. 11b). However, wind backing and veering can be more easily discerned from the wind hodograph—another tool in the WSR-88D product arsenal useful for detecting split fronts and CFAs (Fig. 11d). Both the 0635 UTC radial velocity display and hodograph indicate veering of the winds from a southeasterly direction near the surface to a southwesterly direction at 15 000 ft (4.6 km), followed by ~20° of backing in the 15 000–20 000-ft (4.6–6.1 km) layer. The

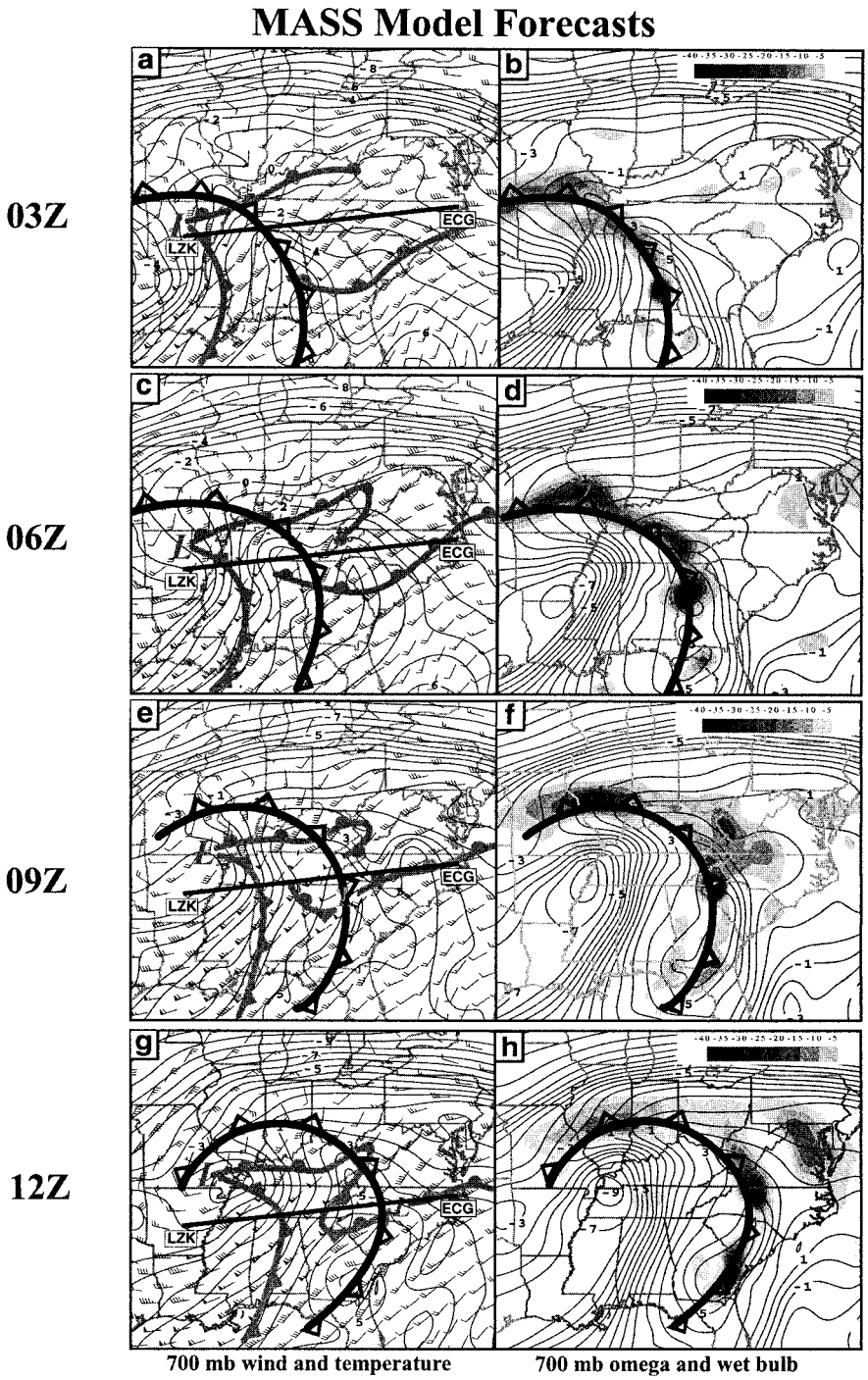

FIG. 6. (a), (c), (e), and (g) MASS model forecasts of 700-hPa winds (same notation as in Fig. 5) and temperatures (solid lines, 1°C intervals) at (0300, 0600, 0900, and 1200 UTC 19 Dec 1995, respectively. (b), (d), (f), and (h) MASS model forecasts of 700-mb upward motions (gray shading, in μbar s^{-1}) and wet-bulb temperatures (solid lines, 1°C intervals) at these same respective times. Surface fronts are shown by standard symbols in gray in the left panels; the split cold front at 700 hPa is shown with black open pips in all panels. The line segment in (a), (c), (e), and (g) shows the position of the vertical cross sections appearing in subsequent figures.

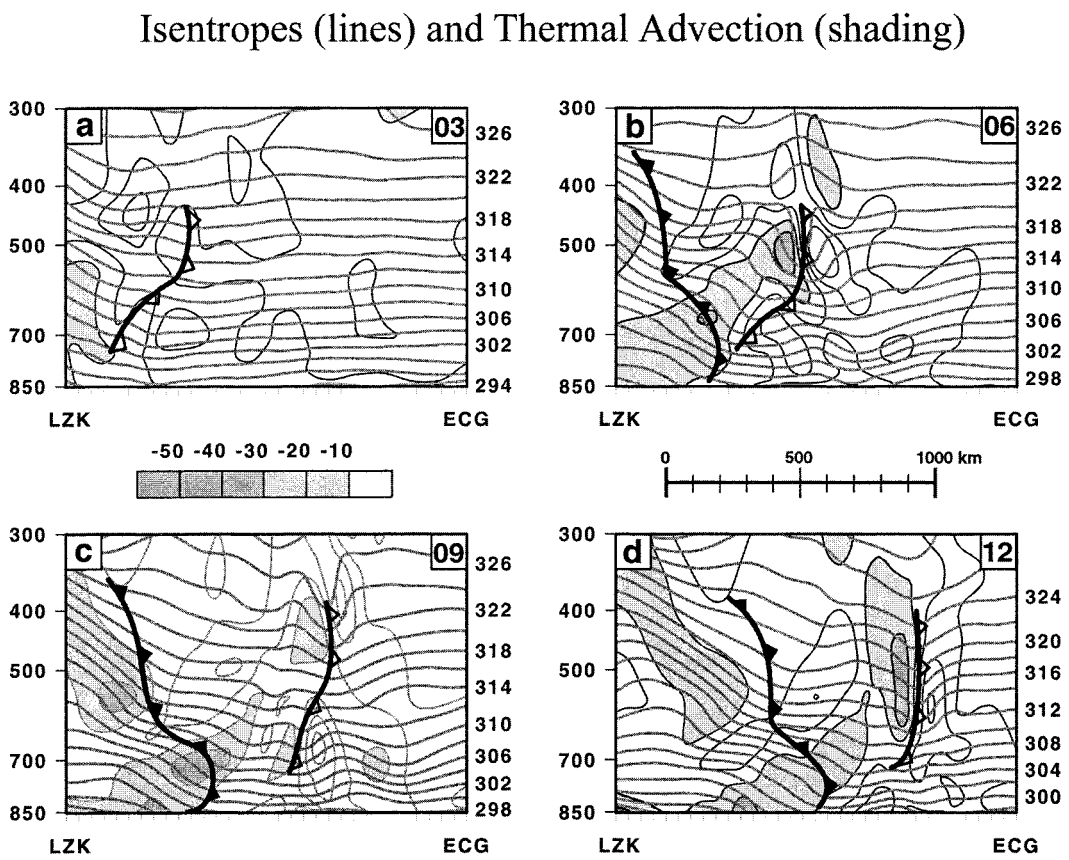

FIG. 7. Vertical cross section from Little Rock, Arkansas (LZK), to Elizabeth City, North Carolina (ECG) (see Fig. 6 for location) of isentropes (gray lines, 2-K intervals) and temperature advection (thin black lines, 10°C day^{-1} contour intervals, with cold advection regions shaded) predicted by the MASS model for (a) 0300, (b) 0600, (c) 0900, and (d) 1200 UTC 19 Dec 1995. Conventional cold front is shown by standard symbols. Split cold front is depicted with open pips.

pattern in Fig. 11b is similar in appearance to the idealized pattern shown in Fig. 11a, though it deviates at the highest levels, in that a return to veering occurs in the KGSP imagery. Nevertheless, it is often difficult to spot such minor backing behavior, particularly if the forecaster is not searching for this feature. Furthermore, the hodograph is only valid for one instant of time, and may be unrepresentative of the general flow features.

Neither the radial velocity display nor the wind hodograph are well suited for detecting *temporal changes* in the vertical profile of the winds that would alert a forecaster to the *passage* of a split front or cold front aloft. Much better suited for this purpose is the VWP, which is a time–height display of the mean horizontal winds using the VAD technique (Klazura and Imy 1993). When the wind is homogeneous at a given altitude, the radial velocity will display a regular sinusoidal behavior as the radar scans azimuthally. The reliability of the estimated wind at each height is measured by the root-mean-square difference from the fitted sine function. As many as 33 wind barbs from 2000 ft above the surface to 15 km can be obtained every 1000 ft (305 m) at 5–10-min intervals. Gaps in the VWP display may result due to a lack of scatterers, when symmetry errors are exceeded in the VAD processing, or when the rms error is too large (such as in the presence of convection). In a comparison of VWP data with nearby rawinsondes for sites in the central and eastern United States, Lee et al. (1994) found that the wind directions differed by $<10°$ in 85% of the cases, and that wind speed differences were <5 kt 75% of the time.

Level-II WSR-88D data were processed using the WSR-88D Algorithm Testing and Display System (Sanger et al. 1995) to obtain VWP displays from the five radar sites mentioned earlier, plus Wakefield, Virginia, and Wilmington, North Carolina. VWP winds with rmse ≤ 4 kt were then written to a file for display using GEMPAK. An example of this processing is shown in Fig. 12 for the KGSP radar for the time period of 0500–0900 UTC. Early in this period, gentle wind veering and strong speed shear are evident. The split-front rainband passes this site shortly after 0600 UTC and continues to produce moderate rainfall for approximately the next hour, during which time several VWP data dropouts are obvious. Wind veering below 3.0 km (10 000 ft) intensifies during this period, while signif-

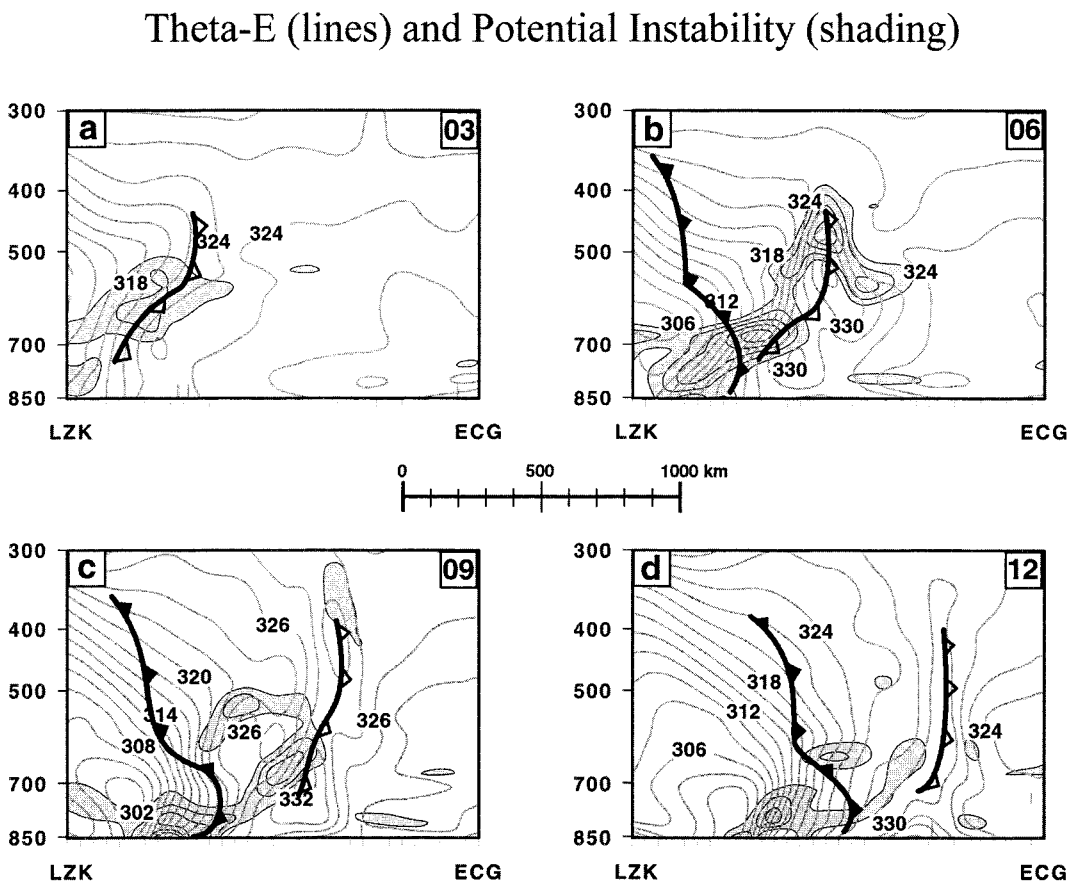

FIG. 8. As in Fig. 7 except depicting equivalent potential temperature (gray lines, 2-K intervals) and regions of potential instability [black lines with shading, 1 K (100 hPa)$^{-1}$].

icant backing of the winds above 4.6 km (15 000 ft) becomes apparent by 0630 UTC in conjunction with the passage of the split front.

VWP data in the form just discussed have limited value for detection of frontal systems above the surface in a forecast office, in part because the wind backing feature is often rather subtle. Furthermore, the extraction of quantitative information from this kind of display is time consuming and impractical in an operational setting. Knowledge of the actual depth, intensity, and time-varying structure of the frontal system can best be obtained from more quantitative methods described below. This ''thermal advection retrieval'' technique can be implemented in real time, provided one has access to the raw moment data in digital form from the WSR-88D Radar Product Generator.

d. Split-front detection from radar thermal advection retrievals

If it can be assumed that the winds obtained from the VWP display are geostrophic ($\mathbf{V} = \mathbf{V}_g$), then the horizontal temperature gradients can be retrieved using the thermal wind equation by assuming that the observed wind shear ($\partial\mathbf{V}/\partial p$) is geostrophic ($\partial\mathbf{V}_g/\partial p$). Under this assumption, application of the thermal wind relationship in isobaric coordinates to the VWP winds can allow for retrieval of the temperature gradient ∇T as follows:

$$\frac{\partial \mathbf{V}}{\partial \ln p} \cong \frac{\partial \mathbf{V}_g}{\partial \ln p} = \frac{-R}{f}\mathbf{k} \times \nabla_p T, \tag{3}$$

where R is the gas constant, p is pressure, and $\mathbf{k}$ the vertical unit vector. Upon taking the cross product of (3), using centered finite differencing in the vertical, and rearranging, we obtain the retrieved temperature gradient with respect to an isobaric surface at a particular geopotential height at a radar site:

$$\nabla_r T(z, t) = \frac{fp}{R}\mathbf{k} \times \frac{\mathbf{V}[p(z + \Delta z), t] - \mathbf{V}[p(z - \Delta z), t]}{2\{[p(z + \Delta z), t] - [p(z - \Delta z), t]\}}. \tag{4}$$

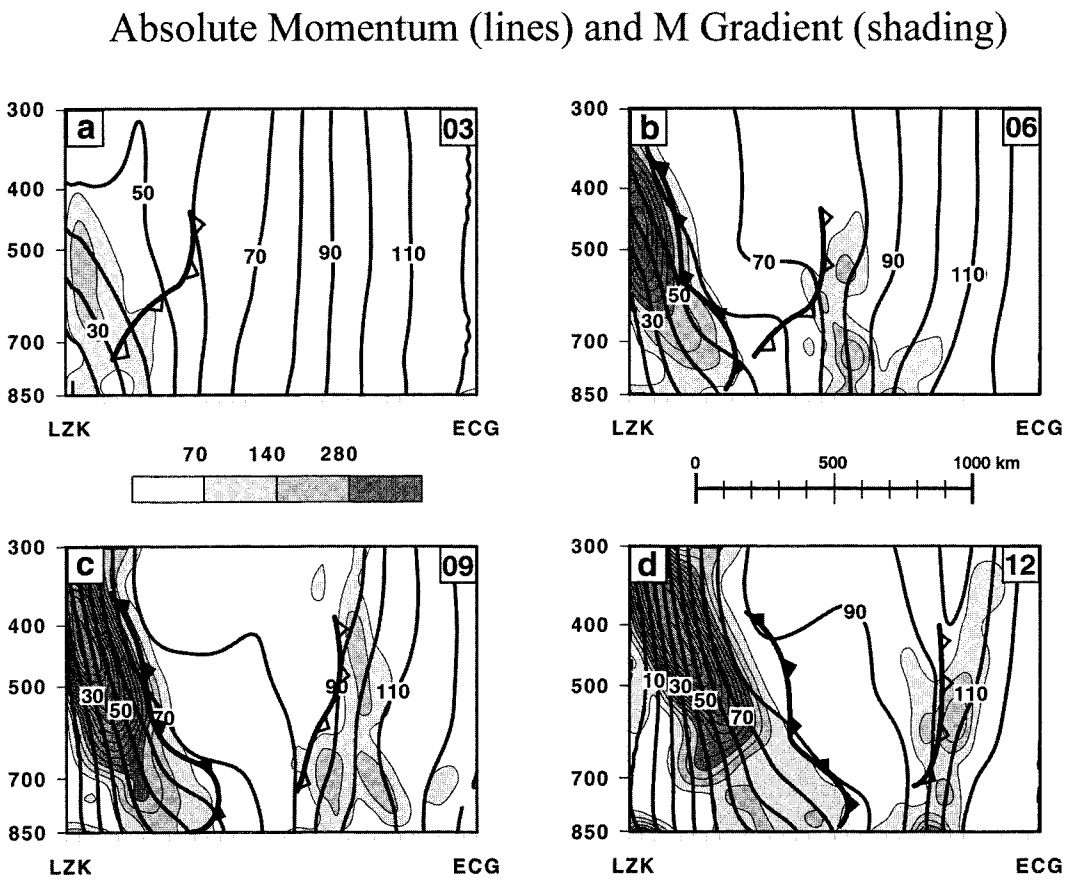

FIG. 9. As in Fig. 7 except depicting absolute geostrophic momentum M_g (black lines, contoured every 10 m s^{-1}). Light, medium, and dark shading indicates regions in which the product $|(\partial M_g/\partial y)(\partial\theta/\partial y)| > 70$, 140, and 280 $\times$ 10^{-11} °C m^{-1} s^{-1}, respectively.

As applied herein, $\mathbf{V}[p(z), t]$ in (4) is the VWP wind velocity at height z and time t, $p(z, t)$ is the corresponding pressure, and $\Delta z = 305$ m is the vertical grid length. The conversion of the VWP winds measured in height coordinates to pressure coordinates is achieved by using the closest observed rawinsonde to the radar site, linearly interpolated in time between the 12-hourly release intervals. Thermal advection is then calculated from the retrieved temperature gradient and the VWP layer-mean wind $\overline{\mathbf{V}} = \mathbf{i}\overline{u} + \mathbf{j}\overline{v}$ as

$$-\overline{\mathbf{V}} \cdot \boldsymbol{\nabla}_r T(z, t) = -\left[\overline{u}(z, t)\frac{\partial T_r(z, t)}{\partial x} + \overline{v}(z, t)\frac{\partial T_r(z, t)}{\partial y}\right]. \quad (5)$$

This thermal wind technique for retrieving horizontal temperature gradients was first developed for a wind profiling radar by Neiman and Shapiro (1989). They discuss how the actual temperature gradient $\boldsymbol{\nabla}T_{ac}$ can deviate from the retrieved temperature gradient $\boldsymbol{\nabla}T_r$ when the wind within the layer of interest is not in geostrophic balance. The general form of the inviscid thermal wind equation in natural coordinates,

$$\boldsymbol{\nabla}_{ac}T = \underbrace{\frac{fp}{R}\mathbf{k} \times \frac{\partial \mathbf{V}}{\partial p}}_{1} + \underbrace{\frac{p|\mathbf{V}|K_t}{R}\mathbf{k} \times \frac{\partial \mathbf{V}}{\partial p}}_{2} + \underbrace{\frac{p}{R}\frac{\partial}{\partial p}(|\mathbf{V}|K_t)\mathbf{k} \times \mathbf{V}}_{3} + \underbrace{\frac{p}{R}\frac{\partial}{\partial p}\left(\mathbf{t}\frac{d|\mathbf{V}|}{dt}\right)}_{4}, \quad (6)$$

shows that $\boldsymbol{\nabla}T_r$ (term 1) is only one of four terms. The second term measures the effect of curvature of the flow. In the presence of vertical wind shear ($\partial\mathbf{V}/\partial p$) and either cyclonic flow ($K_t > 0$) or anticyclonic flow, the retrieved temperature gradient (which ignores this effect) will provide for an inaccurate estimate of the actual temperature gradient $|\boldsymbol{\nabla}T_{ac}|$. However, in either case, the direction of the temperature gradient will be properly determined. Errors can arise in both direction and magnitude of $\boldsymbol{\nabla}T$ when the third term is nonzero. Finally,

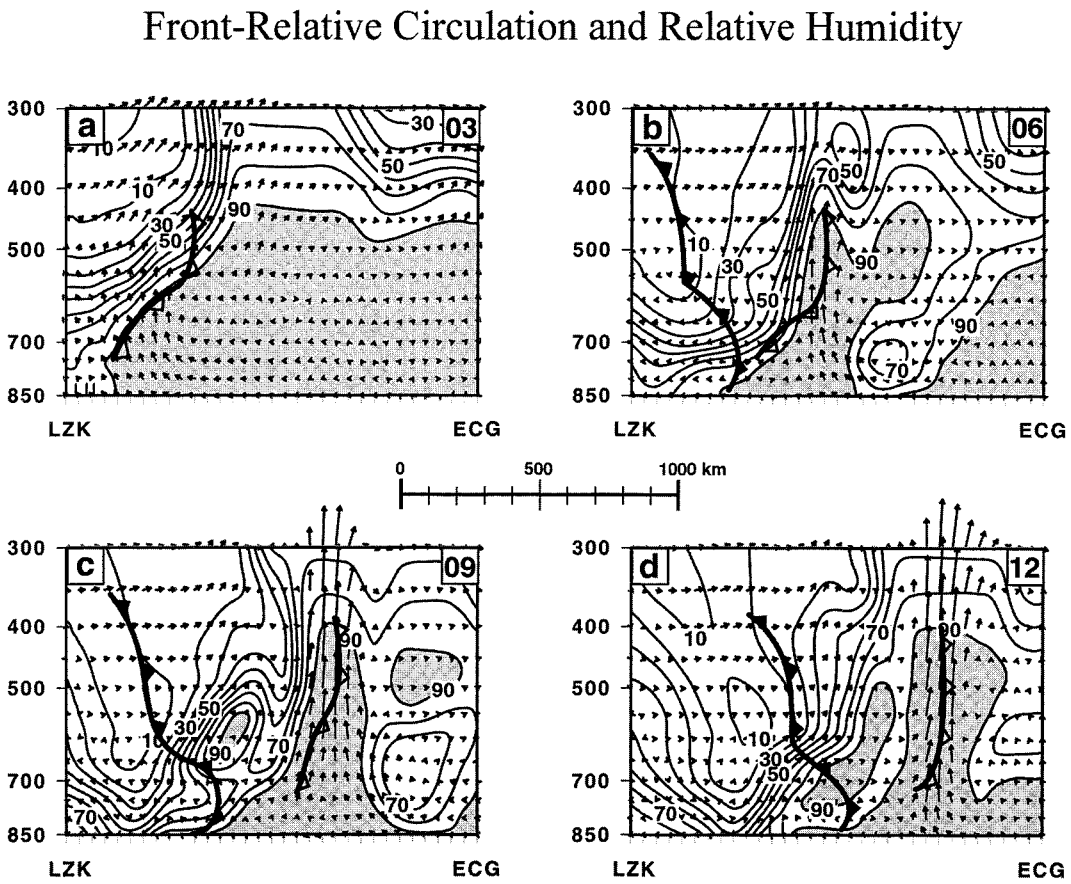

FIG. 10. As in Fig. 7 except depicting circulation relative to the movement of the split cold front (vectors) and regions of relative humidity >90% (shading). Maximum vertical velocities are 80 μbar s^{-1}.

the fourth term accounts for vertical gradients of parcel accelerations. This term can be important for such phenomena as inertia–gravity waves, strong convection, flow within the frictional boundary layer, and at the top of the cold air in CAD events (due to the blocking effect of the Appalachian Mountains).

In the present case, the region affected by the split front was initially dominated by weakly anticyclonic flow, which would introduce an error into ∇T_{ac}. In addition, strongly cyclonic flow occurred at midlevels in the local vicinity of the split front, as may be inferred from the VWP display from KGSP over the interval 0400–1300 UTC (Fig. 13a). On the other hand, the increasing wind speed and cyclonic curvature with height in this same region means that this effect from term 2 was complicated by the effects of term 3. The combined complications arising from terms 2, 3, and 4 represent a source of error in the thermal retrievals in the planetary boundary layer, in the presence of convection, and, unfortunately, in the frontal zone itself.

It is not a simple matter to rigorously account for all the terms in (6). Instead, the best evidence for the validity of this simple retrieval scheme lies in an examination of the meteorological meaningfulness of the results and comparisons drawn with the mesoscale model forecasts of thermal advection. The technique was applied to VWP data from KFFC, KGSP, and KRAX in order to gain an understanding of the changing structure and intensity of the split front as it crossed from Georgia into North Carolina. A two-pass Barnes objective analysis scheme developed by Carr et al. (1995) for use with wind profiler data was adapted for our purposes here. This scheme produces a regular time–height grid of data from the irregularly spaced VWP dataset (caused by data gaps). This interpolation procedure was necessary in order to use the thermal wind equation to retrieve the temperature gradient and thermal advection fields according to (4) and (5), respectively.

Resulting application of the thermal advection retrieval to the KGSP VWP data appears in Fig. 13b. Strong cold advection appears suddenly at 0615 UTC in the midtroposphere, notably the 4.5–6.5-km layer, wherein is found the backing of winds discussed earlier. Pronounced warm advection appears directly beneath this layer, in conjunction with the enhanced wind veering seen in the VWP display. The pattern of cold ad-

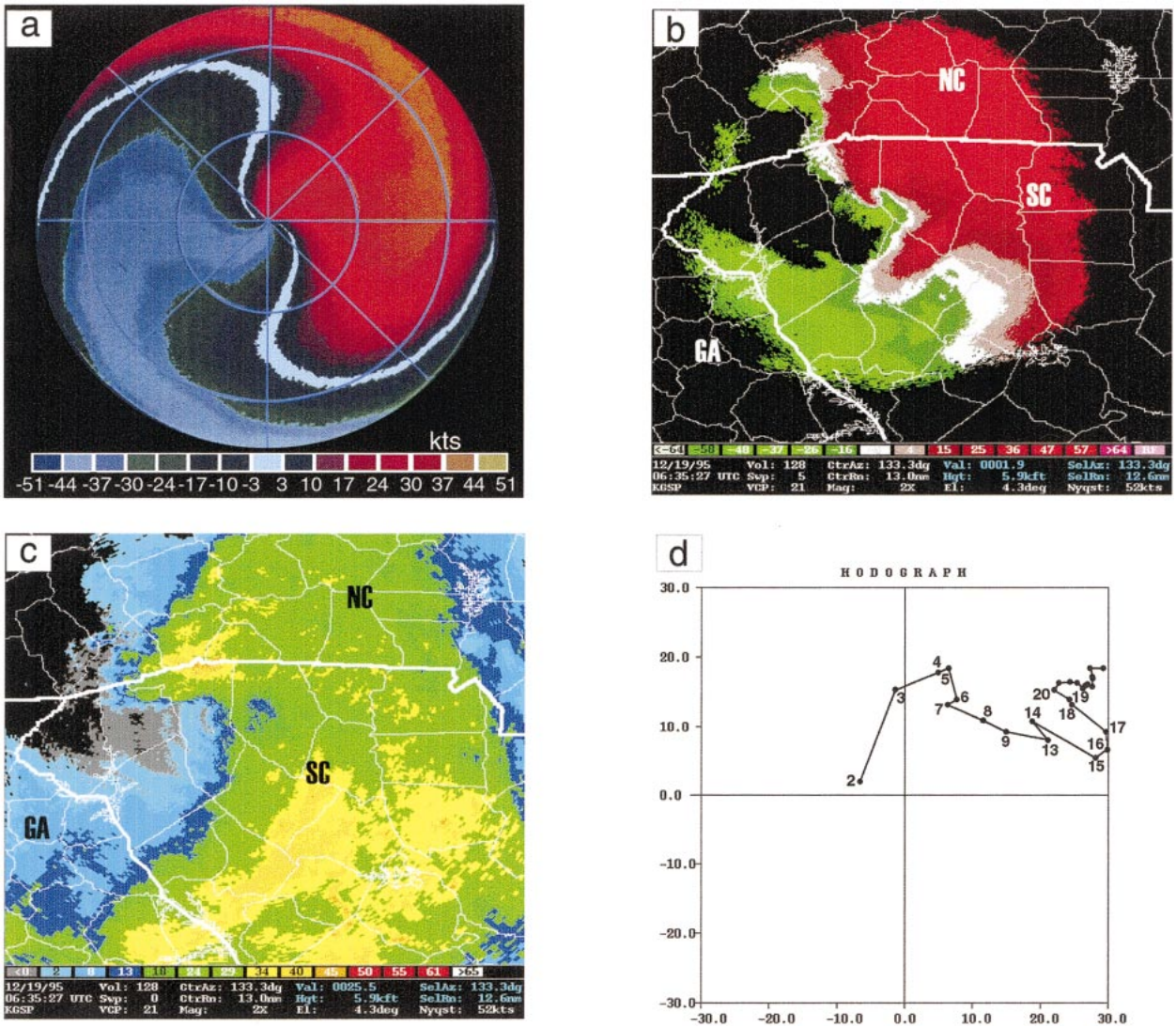

FIG. 11. (a) Radial velocity on radar PPI display for idealized case of lower-level geostrophic warm advection and geostrophic cold advection aloft (after Brown and Wood 1983). (b) and (c) PPI displays at 0635 UTC 19 Dec 1995 from the KGSP WSR-88D radar of radial velocity (m s^{-1}) for 4.3° elevation sweep and composite reflectivity (dBZ), respectively. (d) KGSP wind hodograph at 0635 UTC [numbers are ft above ground level $(1000)^{-1}$]. The split-front rainband is passing just to the east of the radar at this time (cf. Fig. 4b). Inbound velocities (kt) are negative, outbound velocities are positive in (a) and (b).

vection suggests a true frontal structure.[4] It is intriguing that the strongest cold advection exhibits the greatest forward advance in the midtroposphere, relative to that at higher altitudes. Furthermore, the depth of this cold advection does not increase westward (with increasing time), but surprisingly, the greatest depth is found at its leading edge. Another interesting structure in this field is suggested by the occurrence of three individual maxima in cold advection (at 0630, 1015, and 1300 UTC), and corresponding maxima in warm advection beneath two of these regions. These features are separated by 200–275 km, assuming the 72 km h^{-1} propagation speed of the split front applies to all three of them. It is unknown whether these features indicate secondary frontal surges, or something else.

Similar mesoscale features and structures appear in the Atlanta thermal retrieval field (Fig. 14b). The fact that such strong similarity exists between these two independently retrieved fields argues for the validity of the results and suggests that these interesting frontal structures are real. The Atlanta retrievals are the more reliable because data dropouts are less numerous (Fig.

[4] Although there are some small gaps in the data between 0600 and 0700 UTC, the winds below and above these gaps clearly indicate veering, with the backing being confined to altitudes above 4 km, where there is ample data (e.g., at 0630 UTC).

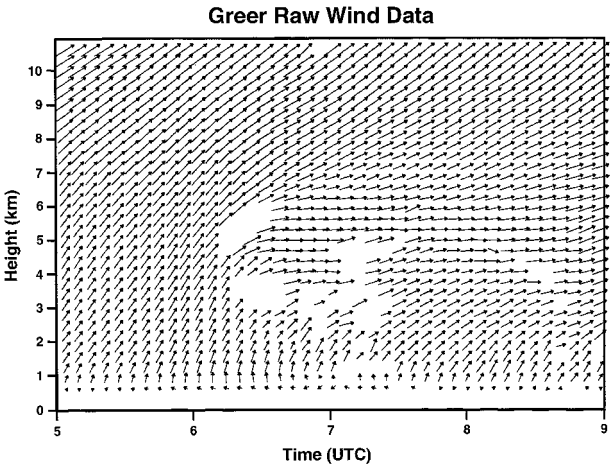

FIG. 12. VWP from KGSP for 0500–0900 UTC 19 Dec 1995. Note presence of backing winds above 4.6 km (15 000 ft) beginning shortly before 0630 UTC. This layer of backing is evident at higher altitudes at later times.

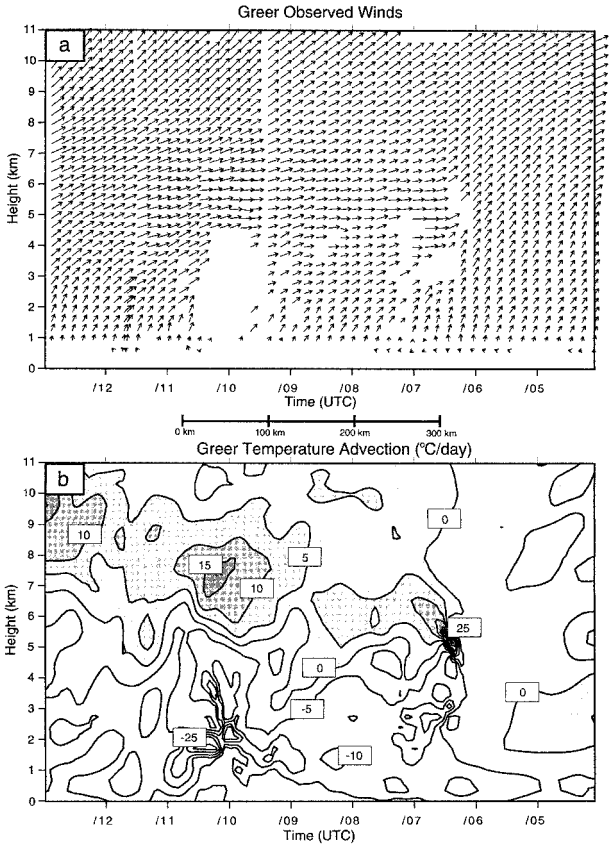

FIG. 13. (a) VWP display from KGSP for 0400–1300 UTC 19 Dec 1995 (time axis is flipped to make it easier to convert time to space, note the length scale), and (b) retrieved time–height analysis of geostrophic thermal advection (°C day^{-1}), with cold advection regions shaded. Leading edge and core of split-front rainband pass KGSP at ~0600 and ~0630 UTC, respectively.

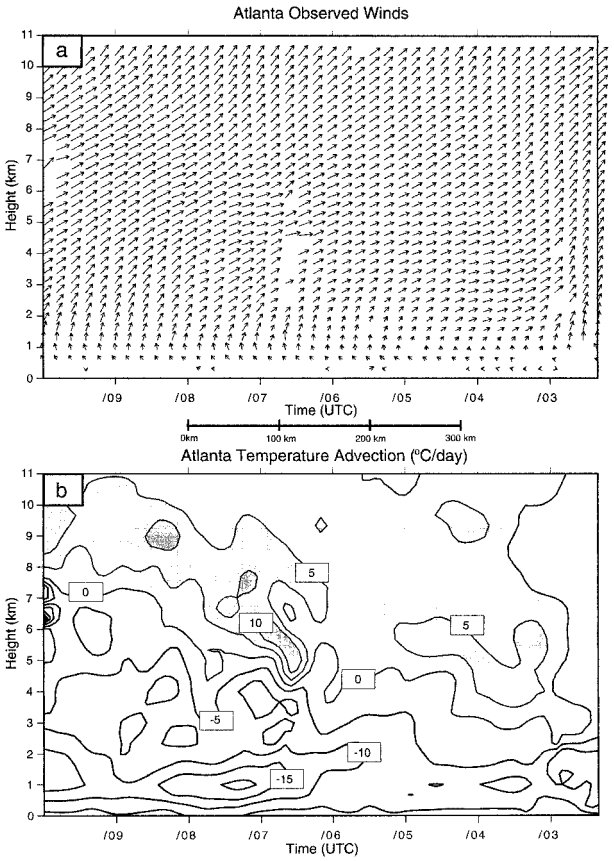

FIG. 14. As in Fig. 13 except for KFFC radar for 0230–1000 UTC 19 Dec 1995. Passage of the split-front rainband occurs between 0300 and 0330 UTC.

14a). One can easily trace the movement of the split front from its passage at Atlanta at 0315 UTC to Greenville–Spartanburg at 0615 UTC. Comparison to the precipitation field (Figs. 4a,b) reveals that the leading edge of the *retrieved* split front (onset of cold advection) lies immediately behind the axis of the *observed* rainband (axis of maximum reflectivity). Note also that this midtropospheric front occurs at least 8 h before the passage of the cold front at the surface.

Examination of the retrieved thermal advection field at Raleigh reveals a very interesting difference in the split front. No longer is a well-defined frontal structure seen. The retrieval gives the impression that the split front is literally disintegrating, since only patches of cold advection can be found at rather high levels (above 4.5 km). This impression is quite consistent with the observed degradation in the structure of the banded precipitation (Figs. 4c,d). These results suggest that there is valuable information contained in these thermal advection fields, despite the gross simplification of geostrophy implicit in the retrieval process. Furthermore, it would seem that such information could be used to closely monitor the progress and morphology of split fronts and CFAs in real time.

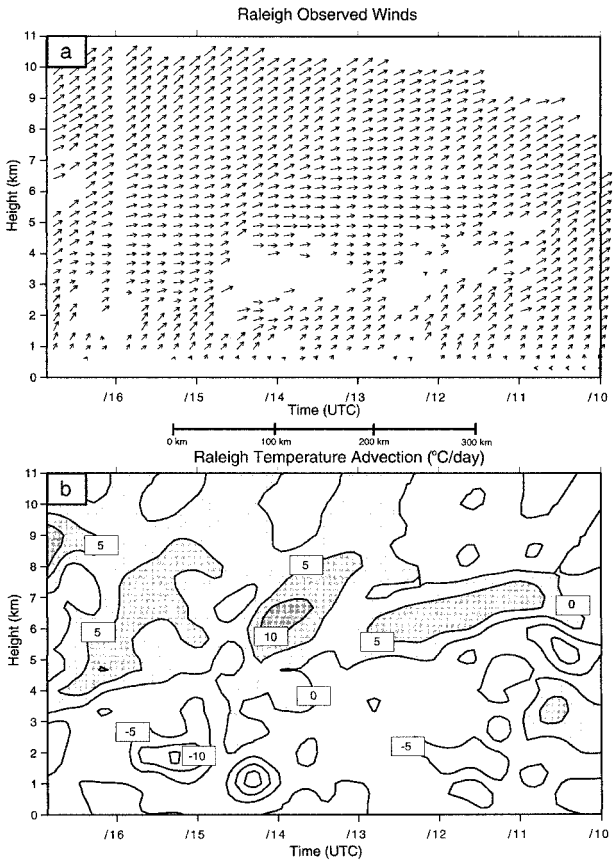

FIG. 15. As in Fig. 13 except for KRAX radar for 1000–1645 UTC 19 Dec 1995. Passage of the remnant split-front rainband occurs at ~1100 UTC, but is poorly defined.

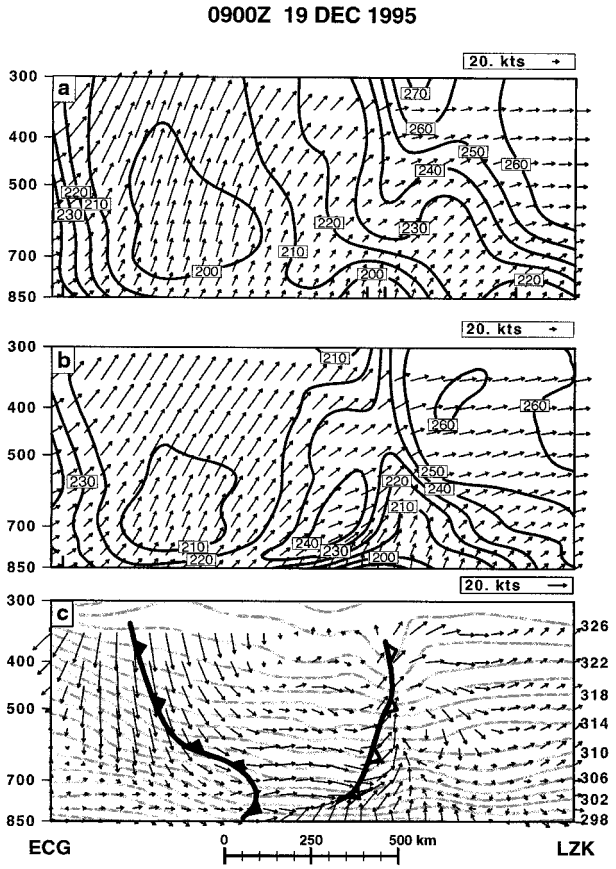

FIG. 16. Vertical cross section from LZK to ECG of (a) geostrophic wind vectors and directions (lines), (b) total wind vectors and directions (lines), and (c) ageostrophic wind vectors and isentropes (gray lines) predicted by the MASS model for 0900 UTC 19 Dec 1995. Conventional cold front is shown by standard symbols. Split cold front is depicted with open pips. The predicted wind fields in (b) should be compared to the observed wind vector field obtained from the KGSP radar (Fig. 13a).

Nevertheless, it is imperative to seek additional measures of the validity of these fields beyond the yardsticks of meteorological meaningfulness and time–space continuity. Since no other independent data source exists for such verification purposes, the next best thing is to compare the retrieved temperature advection fields to those forecast by a mesoscale model. A time-to-space conversion of these time–height fields (note the distance scales in Figs. 13–15) can be compared for this purpose to the MASS model vertical cross sections of thermal advection (Fig. 7). Good agreement is found in that the split front in both the model and the retrieved fields is most pronounced in the 4.0–6.5-km layer (650–450 hPa). In addition, this front is found 400–600 km ahead of the deep tropospheric front in both the model and retrieved fields. A significant discrepancy is that the ''dipole'' feature in the model fields is not apparent in the retrieved fields; rather, warm advection occurs *beneath* the maximum in the retrieved cold advection. Another difference is that the 3–4-hourly (216–288 km) mesoscale structures in the retrieved fields are not obvious in the model forecasts. Finally, the disintegration in the retrieved thermal advection fields at Raleigh (Fig. 15b) does not occur in the model forecast for 1200 UTC (Fig. 7d), which is when the simulated split front is nearest to Raleigh.

The horizontal winds forecast by the model (Fig. 16b) were also compared to those obtained directly from the VWP (Fig. 13a). Wind veering ahead of the split front is obvious in both the model and VWP display. The backing wind signature of the split front is also seen in both fields, though in the model the low-level veering (from 210° to 245°) is more obvious than the backing from 245° at 700 hPa to 220° at 350 hPa. However, is this backing associated with the geostrophic wind, which is assumed by the retrieval scheme? If one believes the model, the answer to this question is in the negative (Fig. 16a), since all the backing is attributable to the ageostrophic wind (Fig. 16c). In fact, the signature of the presence of the split front in the model is entirely that of the ageostrophic transverse circulation associated with the frontogenesis process. Whether this is also true in observations cannot be determined, but whatever the

case may be, the retrieval scheme does an excellent job in defining the presence of the split front.

4. Discussion and conclusions

One of the most difficult and important forecast challenges in the Carolinas, Virginia, and Georgia is the evolution and demise of cold air damming. Forecasts of surface temperature can be wrong by 20°C, as the forecast of a pleasant day turns out to be embarrassed by the reality of a dreary overcast situation in which the issue suddenly becomes whether the steady precipitation that is falling will be in the liquid or solid form. Numerous mechanisms can help to maintain or erode this shallow layer of cold air, but one that has not received much attention is the passage of a cold frontal system aloft over the cold air damming region. The competing effects of evaporational cooling of falling precipitation into a dry subcloud layer and warming in response to the release of latent heat in the split front rainband have never been determined.

In the present case, surface temperatures in North Carolina remained virtually constant during the passage of a split-front rainband, and the cold air damming remained intact. Maintenance of this shallow region of cold air occurred despite the fact that the atmosphere was saturated throughout a deep column, so that subcloud evaporational cooling was negligible. On the other hand, the mesoscale model used in this study (MASS) removed the cold air prematurely in response to the development of a fictitious surface cyclone along the southern boundary of the cold air. This cyclone occurred because of strong latent heat release and the associated development of vorticity in the midtroposphere. An isallobaric fall center occurred just ahead of this mesoscale cyclone along the coastal front. The convergent isallobaric flow caused a reformation of the front inland over the Carolina Piedmont in response to the forced frontogenesis northeast of the cyclone, leading to the sudden erosion of the cold air. Thus, this forecast error was ultimately tied to problems in handling the convective precipitation.

Nevertheless, a well-organized band of convection actually did occur over the cold air north of the warm front (coastal front) and well ahead of the surface cold front, which was advancing eastward along the Gulf Coast states. This intense rainband was produced by a split cold front that passed over the warm front, and entered the cold air damming region in northern Georgia and western South Carolina with little reduction in intensity. The split front in the MASS model was revealed by a coherent, arc-shaped band of upward motion along the leading edge of a strong horizontal gradient in the 700-hPa wet-bulb temperature, ~400 km ahead of the surface cold front. As this midtropospheric front passed over the surface warm front and into the cold air damming region, vertical cross-section analyses of equivalent potential temperature showed that the split front created a deep, elevated layer of potential instability. In addition, the split front produced an efficient lifting mechanism—an ageostrophic, thermally direct circulation—for releasing this instability as elevated deep convection. Unfortunately, the model maintained the convection for too long as the split front advanced into North Carolina, causing the problem with the erroneous surface cyclone.

On the other hand, the operational Eta Model forecast[5] displayed only a weak signature of the split front. The 6-h forecasts from the 80-km Eta model valid at 0600 UTC are presented in Fig. 17 for comparison with the MASS model forecasts in Figs. 6, 7, and 10. Note in particular the lack of a coherent arc-shaped band of upward motion along the split front, although there are broad areas of ascent, primarily along the northern side of the split front. Furthermore, the thermal advection dipole in the cross section is lacking, though the isentropes do display a forward-sloping structure characteristic of split fronts and there is strong ascent in the upper troposphere (curiously, this occurs above the analyzed split front).

An S–inverted S pattern in the zero isodop on WSR-88D radial velocity displays from KFFC and KGSP clearly denoted the passage of the split front at these two locations. This isodop pattern implies the presence of wind backing above wind veering, thus, of geostrophic cold advection at midlevels overlying warm advection. The changing structure of the split front was deduced from temperature advection patterns retrieved from the VWP time–height display. The thermal retrieval scheme is based on the simplifying assumption that the observed winds in the VWP display are geostrophic. Results showed a region of strong geostrophic cold advection in the 4.5–6.5-km layer associated with backing winds, consistent with the MASS model. The diagnosed split front from KFFC and KGSP displayed a forward-sloping structure with the greatest depth of cold advection being at the leading edge of the front, followed by several mesoscale surges or reinforcements of cold air. The convective rainband was located just ahead of this split front. As the front propagated into North Carolina, this well-defined frontal structure disintegrated; interestingly, the convective band also became disorganized.

Results from the thermal advection retrieval were found to be meaningful and to exhibit excellent time–space continuity. Comparison of the retrieved advection fields to those forecast by the mesoscale model showed good overall agreement, though details differed. On the other hand, the MASS model forecast indicated that all

[5] The 32-km Eta Model of today was not available for the 1995 case study here. Our recent attempts to use this mesoscale version of the Eta Model for prediction of split fronts have met with remarkable success (unpublished). The present study indicates that 80-km resolution models like that available for this study are not ideally suited for this application.

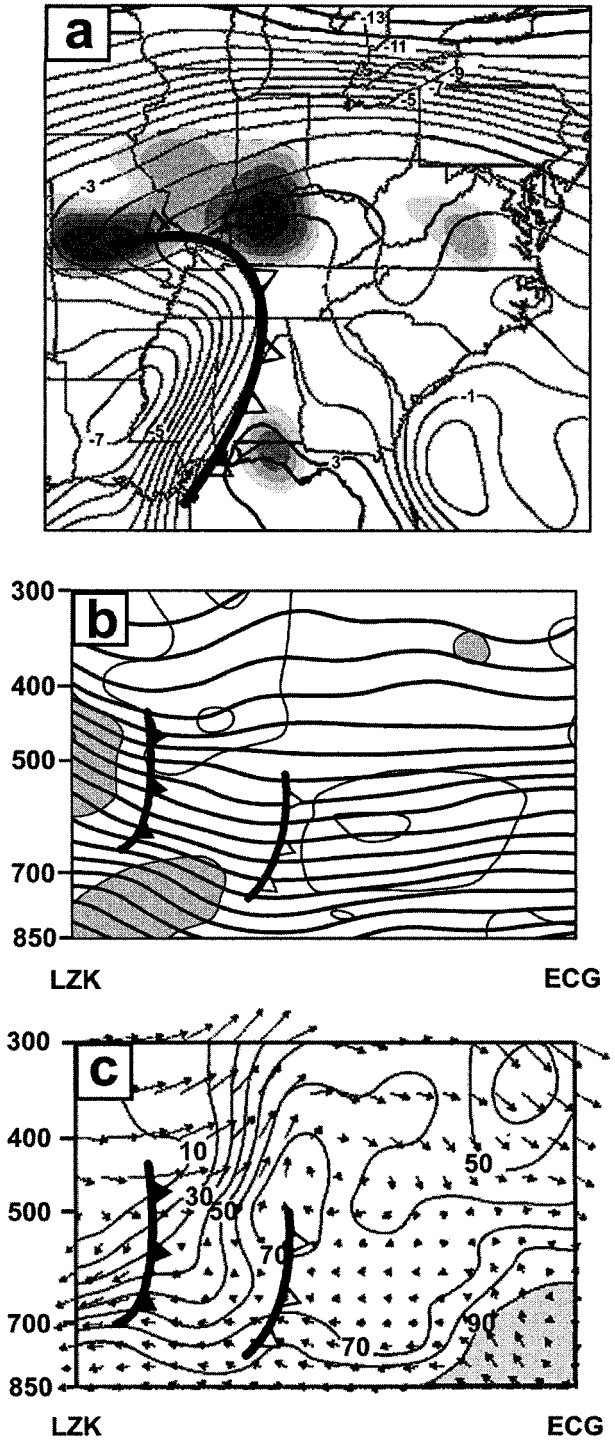

FIG. 17. Eta Model 6-h forecasts valid at 0600 UTC 19 Dec 1995 of (a) 700-hPa upward motions and wet-bulb temperatures (as in Fig. 6), (b) isentropic cross section with superposed thermal advection patterns (as in Fig. 7), and (c) frontal circulation system and relative humidity (as in Fig. 10).

of the backing of the winds was attributable to the ageostrophic winds associated with the frontal transverse circulation system. Although the assumptions underlying the retrieval scheme may thus be questioned, nevertheless its ability to define the presence and structure of the front was demonstrated. It is recommended that this thermal advection retrieval be developed and tested for real-time application within National Weather Service offices that have the ability to feed the data from the Radar Product Generator to an offline computer for processing. The general validity and utility of this simple approach can then be evaluated. Future research should also consider the use of the full divergence equation to retrieve the geopotential height and hydrostatic temperature fields from multiple WSR-88D radars, similar to what has been done with a network of wind profilers. However, its real-time implementation must await vastly improved means for accessing the level-II data from multiple radar sites.

Acknowledgments. Lisa Gray, Rob Gilliam, Jamie Mitchem, and Michael Brennan provided valuable assistance in the preparation of figure graphics and GEMPAK analyses. Tony Krogh and Jeremy Moore contributed to the development and application of the thermal retrieval software. Ken Waight implemented the version of the MASS model used in this study. Comments provided by John Locatelli and Mark Stoelinga were helpful for clarifying concepts. Funding for this research was obtained from the National Science Foundation under ATM-9700626 and COMET Outreach Project Grant S96-75675.

REFERENCES

Bell, G. D., and L. F. Bosart, 1988: Appalachian cold-air damming. *Mon. Wea. Rev.,* **116,** 137–161.

Bosart, L. F., C. J. Vaudo, and J. H. Helsdon Jr., 1972: Coastal frontogenesis. *J. Appl. Meteor.,* **11,** 1236–1258.

Brown, R. A., and V. T. Wood, 1983: Improved severe storm warnings using Doppler radar. *Natl. Wea. Dig.,* **8,** 17–27.

Browning, K. A., 1985: Conceptual models of precipitation systems. *Meteor. Mag.,* **114,** 293–319.

——, and G. A. Monk, 1982: A simple model for the synoptic analysis of cold fronts. *Quart. J. Roy. Meteor. Soc.,* **108,** 435–452.

——, and N. M. Roberts, 1996: Variation of frontal and precipitation structure along a cold front. *Quart. J. Roy. Meteor. Soc.,* **122,** 1845–1872.

Businger, S., W. H. Bauman III, and G. F. Watson, 1991: The development of the Piedmont front and associated outbreak of severe weather on 13 March 1986. *Mon. Wea. Rev.,* **119,** 2224–2251.

Carlson, T. N., 1980: Airflow through midlatitude cyclones and the comma cloud pattern. *Mon. Wea. Rev.,* **108,** 1498–1509.

Carr, F. H., P. L. Spencer, C. A. Doswell, and J. D. Powell, 1995: A comparison of two objective analysis techniques for profiler time height data. *Mon. Wea. Rev.,* **123,** 2161–2180.

Cotton, W. R., G. Thompson, and P. W. Mielke Jr., 1994: Real-time mesoscale prediction on workstations. *Bull. Amer. Meteor. Soc.,* **75,** 349–362.

Crawford, M. E., 1950: A synoptic study of squall lines. *Bull. Amer. Meteor. Soc.,* **31,** 351–357.

Eliassen, A., 1962: On the vertical circulation in frontal zones. *Geofys. Publ.,* **24,** 147–160.

Forbes, G. S., R. A. Anthes, and D. W. Thompson, 1987: Synoptic and mesoscale aspects of an Appalachian ice storm associated with cold-air damming. *Mon. Wea. Rev.,* **115,** 564–591.

Fritsch, J. M., J. Kapolka, and P. A. Hirschberg, 1992: The effects of subcloud-layer diabatic processes on cold air damming. *J. Atmos. Sci.,* **49,** 49–70.

Gurka, J. J., E. P. Auciello, A. F. Gigi, J. S. Waldstreicher, K. K. Keeter, S. Businger, and L. G. Lee, 1995: Winter weather forecasting throughout the eastern United States. Part II: An operational perspective of cyclogenesis. *Wea. Forecasting,* **10,** 21–41.

Hobbs, P. V., J. D. Locatelli, and J. E. Martin, 1990: Cold fronts aloft and the forecasting of precipitation and severe weather east of the Rocky Mountains. *Wea. Forecasting,* **5,** 613–626.

Kaplan, M. L., J. W. Zack, V. C. Wong, and J. J. Tuccillo, 1982: Initial results from a mesoscale atmospheric simulation system and comparisons with the AVE-SESAME I data set. *Mon. Wea. Rev.,* **110,** 1564–1590.

Keeter, K. K., S. Businger, L. G. Lee, and J. S. Waldstreicher, 1995: Winter weather forecasting throughout the eastern United States. Part III: The effects of topography and the variability of winter weather in the Carolinas and Virginia. *Wea. Forecasting,* **10,** 42–60.

Keyser, D., and M. A. Shapiro, 1986: A review of the structure and dynamics of upper-level frontal zones. *Mon. Wea. Rev.,* **114,** 452–499.

Klazura, G. E., and D. A. Imy, 1993: A description of the initial set of analysis products available from the NEXRAD WSR-88D system. *Bull. Amer. Meteor. Soc.,* **74,** 1293–1311.

Koch, S. E., M. desJardins, and P. Kocin, 1983: An interactive Barnes objective map analysis scheme for use with satellite and conventional data. *J. Climate Appl. Meteor.,* **22,** 1487–1503.

——, W. C. Skillman, P. J. Kocin, P. J. Wetzel, K. F. Brill, D. A. Keyser, and M. C. McCumber, 1985: Synoptic scale forecast skill and systematic errors in the MASS 2.0 model. *Mon. Wea. Rev.,* **113,** 1714–1737.

Lee, R. R., J. L. Ingram, and G. E. Klazura, 1994: A comparison of data from the WSR-88D VAD wind profile product and rawinsondes at twelve sites—Preliminary results. Postprints, *First WSR-88D Users' Conf.,* Norman, OK, 55–61. [Available from NOAA/WSR-88D Operational Support Facility, 1313 Halley Circle, Norman, OK 73069.]

Locatelli, J. D., J. M. Sienkiewicz, and P. V. Hobbs, 1989: Organization and structure of clouds and precipitation on the mid-Atlantic coast of the United States. Part I: Synoptic evolution of a frontal system from the Rockies to the Atlantic Coast. *J Atmos. Sci.,* **46,** 1327–1348.

——, J. E. Martin, J. A. Castle, and P. V. Hobbs, 1995: Structure and evolution of winter cyclones in the central United States and their effects on the distribution of precipitation. Part III: The development of a squall line associated with weak cold frontogenesis aloft. *Mon. Wea. Rev.,* **123,** 2641–2662.

Manobianco, J., S. E. Koch, V. M. Karyampudi, and A. J. Negri, 1994: The impact of assimilating satellite-derived precipitation rates on numerical simulations of the ERICA IOP 4 cyclone. *Mon. Wea. Rev.,* **122,** 341–365.

——, J. W. Zack, and G. E. Taylor, 1996: Workstation-based real-time mesoscale modeling designed for weather support to operations at the Kennedy Space Center and Cape Canaveral Air Station. *Bull. Amer. Meteor. Soc.,* **77,** 653–672.

Martin, J. E., J. D. Locatelli, and P. V. Hobbs, 1990: Organization and structure of clouds and precipitation on the mid-Atlantic coast of the United States. Part III: The evolution of a mid-tropospheric cold front. *Mon. Wea. Rev.,* **118,** 195–217.

——, ——, and ——, 1992: Organization and structure of clouds and precipitation on the mid-Atlantic coast of the United States. Part V: The role of an upper-level front in the generation of a rainband. *J. Atmos. Sci.,* **49,** 1293–1303.

Mass, C. F., and Y.-H. Kuo, 1998: Regional real-time numerical weather prediction: Current status and future potential. *Bull. Amer. Meteor. Soc.,* **79,** 253–263.

Neiman, P. J., and M. A. Shapiro, 1989: Retrieving horizontal temperature gradients and advections from single-station wind profiler observations. *Wea. Forecasting,* **4,** 222–233.

——, F. M. Ralph, M. A. Shapiro, B. F. Smull, and D. Johnson, 1998: An observational study of fronts and frontal mergers over the continental United States. *Mon. Wea. Rev.,* **126,** 2521–2554.

Reed, R. J., 1955: A study of a characteristic type of upper-level frontogenesis. *J. Meteor.,* **12,** 226–237.

——, and E. F. Danielsen, 1959: Fronts in the vicinity of the tropopause. *Arch. Meteor. Geophys. Bioklimatol.,* **A11,** 1–11.

Richwein, B. A., 1980: The damming effect of the southern Appalachians. *Natl. Wea. Dig.,* **5,** 2–12.

Riordan, A. J., 1990: Examination of the mesoscale features of the GALE coastal front of 24–25 January 1986. *Mon. Wea. Rev.,* **118,** 258–282.

Rogers, E., D. G. Deaven, and G. J. DiMego, 1995: The regional analysis system for the operational ''early'' Eta Model: Original 80-km configuration and recent changes. *Wea. Forecasting,* **10,** 810–825.

——, T. L. Black, D. G. Deaven, G. J. DiMego, Q. Zhao, M. Baldwin, N. W. Junker, and Y. Lin, 1996: Changes to the operational ''early'' Eta analysis/forecast system at the National Centers for Environmental Prediction. *Wea. Forecasting,* **11,** 391–413.

Sanger, S. S., R. M. Steadham, J. M. Jarboe, R. E. Schiegel, and A. Sellakannu, 1995: Human factor contributions to the evolution of an interactive Doppler radar and weather detection algorithm display system. Preprints, *11th Int. Conf. on Interactive Information and Processing Systems for Meteorology, Oceanography, and Hydrology,* Dallas, TX, Amer. Meteor. Soc., 1–6.

Shapiro, M. A., 1981: Frontogenesis and geostrophically forced secondary circulations in the vicinity of jet stream-frontal zone systems *J. Atmos. Sci.,* **38,** 954–973.